The host galaxies of Type Ia supernovae discovered by the Palomar Transient Factory

Y.-C. Pan,[1]⋆ M. Sullivan,[2] K. Maguire,[1] I. M. Hook,[1,3] P. E. Nugent,[4,5]
D. A. Howell,[6,7] I. Arcavi,[8] J. Botyanszki,[5,9] S. B. Cenko,[10,11] J. DeRose,[9]
H. K. Fakhouri,[9,12] A. Gal-Yam,[8] E. Hsiao,[13] S. R. Kulkarni,[14] R. R. Laher,[15]
C. Lidman,[16] J. Nordin,[12,17] E. S. Walker[18] and D. Xu[19]

[1]*Department of Physics (Astrophysics), University of Oxford, DWB, Keble Road, Oxford OX1 3RH, UK*
[2]*School of Physics and Astronomy, University of Southampton, Southampton, SO17 1BJ, UK*
[3]*INAF Osservatorio Astronomico di Roma, via Frascati, 33, I-00040 Monte Porzio Catone, Roma, Italy*
[4]*Department of Astronomy, University of California, Berkeley, CA 94720-3411, USA*
[5]*Computational Cosmology Center, Lawrence Berkeley National Laboratory, 1 Cyclotron Road, Berkeley, CA 94720, USA*
[6]*Las Cumbres Observatory Global Telescope Network, Goleta, CA 93117, USA*
[7]*Department of Physics, University of California, Santa Barbara, CA 93106-9530, USA*
[8]*Department of Particle Physics and Astrophysics, Weizmann Institute of Science, Rehovot 76100, Israel*
[9]*Department of Physics, University of California Berkeley, 366 LeConte Hall MC 7300, Berkeley, CA 94720-7300, USA*
[10]*Astrophysics Science Division, NASA Goddard Space Flight Center, Mail Code 661, Greenbelt, MD 20771, USA*
[11]*Joint Space Science Institute, University of Maryland, College Park, Maryland 20742, USA*
[12]*Physics Division, Lawrence Berkeley National Laboratory, 1 Cyclotron Road, Berkeley, CA 94720, USA*
[13]*Carnegie Observatories, Las Campanas Observatory, Casilla 601, La Serena, Chile*
[14]*Division of Physics, Mathematics, and Astronomy, California Institute of Technology, Pasadena, CA 91125, USA*
[15]*Spitzer Science Center, California Institute of Technology, M/S 314-6, Pasadena, CA 91125, USA*
[16]*Australian Astronomical Observatory, PO Box 915, North Ryde NSW 1670, Australia*
[17]*Space Sciences Laboratory, University of California Berkeley, 7 Gauss Way, Berkeley, CA 94720, USA*
[18]*Department of Physics, Yale University, PO Box 208120, New Haven, CT 06520-8120, USA*
[19]*Dark Cosmology Centre, Niels Bohr Institute, University of Copenhagen, Juliane Maries Vej 30, DK-2100 København Ø, Denmark*

ABSTRACT

We present spectroscopic observations of the host galaxies of 82 low-redshift Type Ia supernovae (SNe Ia) discovered by the Palomar Transient Factory. We determine star formation rates, gas-phase/stellar metallicities, and stellar masses and ages of these objects. As expected, strong correlations between the SN Ia light-curve width (stretch) and the host age/mass/metallicity are found: fainter, faster declining events tend to be hosted by older/massive/metal-rich galaxies. There is some evidence that redder SNe Ia explode in higher metallicity galaxies, but we found no relation between the SN colour and host galaxy extinction based on the Balmer decrement, suggesting that the colour variation of these SNe does not primarily arise from this source. SNe Ia in higher mass/metallicity galaxies also appear brighter after stretch/colour corrections than their counterparts in lower mass hosts, and the stronger correlation is with gas-phase metallicity suggesting this may be the more important variable. We also compared the host stellar mass distribution to that in galaxy-targeted SN surveys and the high-redshift untargeted Supernova Legacy Survey (SNLS). SNLS has many more low-mass galaxies, while the targeted searches have fewer. This can be explained by an evolution in the galaxy stellar mass function, coupled with an SN delay-time distribution proportional to t^{-1}. Finally, we found no significant difference in the mass–metallicity relation of our SN Ia hosts compared to field galaxies, suggesting any metallicity effect on the SN Ia rate is small.

Key words: supernovae: general – cosmology: observations – distance scale.

⋆ E-mail: Yen-Chen.Pan@astro.ox.ac.uk

1 INTRODUCTION

Type Ia supernovae (SNe Ia) are remarkable cosmological standardizable candles that are routinely used to measure cosmological parameters (Riess et al. 1998; Perlmutter et al. 1999; Riess et al. 2007; Kessler et al. 2009; Sullivan et al. 2011b; Suzuki et al. 2012). As these studies become increasingly more precise, systematic uncertainties become a significant component of the error budget (Conley et al. 2011). Thus, an important consideration in their future use is the degree to which SN Ia properties evolve with redshift or depend on their environment – and how well any evolutionary effects can be controlled.

The host galaxies and environments of SNe Ia has long been a profitable route to probe astrophysical effects in the SN Ia population, with the observed properties of SNe Ia known to correlate with the physical parameters of their host galaxy stellar populations. SNe Ia in elliptical or passively evolving galaxies are intrinsically fainter than SNe Ia in spiral or star-forming galaxies, and possess narrower, faster evolving (or lower 'stretch') light curves (Hamuy et al. 1995, 1996, 2000; Riess et al. 1999; Howell 2001; Gallagher et al. 2005; Sullivan et al. 2006). The impact of these effects on the cosmological results is small due to observed correlations between SN Ia light-curve shape and luminosity (Phillips 1993), and between SN Ia optical colour and luminosity (Riess, Press & Kirshner 1996; Tripp 1998). When these empirical relations are applied to SN Ia data sets, only small correlations remain between SN Ia luminosity and host galaxy properties, such as their stellar masses or star formation rates (SFR; Kelly et al. 2010; Lampeitl et al. 2010; Sullivan et al. 2010).

These residual trends between SN luminosity and host galaxy properties can be accounted for at the level required by current cosmological analyses, either by directly using host galaxy information in the cosmological fits (Sullivan et al. 2011b) or by applying probabilistic corrections to the absolute magnitudes of the SNe (Suzuki et al. 2012). However, as the size of other systematic uncertainties in the cosmological analyses are reduced as, for example, the accuracy of the photometric calibration procedures improve (Betoule et al. 2013), understanding the physical origin of these astrophysical correlations will become critical for future, larger samples (e.g. Dark Energy Survey; Bernstein et al. 2012).

The two primary competing ideas are that either progenitor metallicity or progenitor age (or a combination of both) play a role in controlling SN Ia luminosities – but directly measuring either is extremely difficult. Indirect information can be obtained on metallicity from the ultraviolet (UV) SN spectra (e.g. Hoeflich, Wheeler & Thielemann 1998; Lentz et al. 2000), and while this has provided useful insights into evolution within SN Ia populations (Ellis et al. 2008; Foley et al. 2008, 2012; Maguire et al. 2012), the interpretation of any individual event is extremely complex even with very high quality data (Mazzali et al. 2013). There is currently no technique to estimate the age of the progenitor star from the SN spectrum.

Thus, many studies have instead focused on detailed spectroscopic studies of the host galaxies of the SNe Ia rather than the events themselves, assembling statistical samples with which to search for correlations between the physical parameters defining the host galaxies, and the SN Ia properties. Such global host galaxy properties are believed to represent reasonable tracers of the SN progenitor star, at least in a statistical sense (Bravo & Badenes 2011). Common spectroscopic measurements include SFRs and gas-phase metallicity measured from nebular emission lines (Gallagher et al. 2005; D'Andrea et al. 2011; Stanishev et al. 2012; Childress et al.

2013b; Johansson et al. 2013; Rigault et al. 2013), and stellar metallicity and age measured from spectral absorption indices (Gallagher et al. 2008; Stanishev et al. 2012; Johansson et al. 2013).

A number of intriguing results have arisen from these studies. Based on star formation activity in the host galaxy, brighter SNe Ia were found to explode in more active galaxies than those in passive galaxies. The SN Ia luminosities were also found to be significantly correlated with host gas-phase metallicities, with metal-rich galaxies tending to host fainter SNe Ia than metal-poor galaxies. A similar trend has also been identified with host stellar metallicity. The stellar age of the host galaxies also shows a correlation with SN Ia luminosities, in the sense that fainter SNe Ia preferentially explode in older populations.

In this paper, we present new spectroscopic observations of the host galaxies of SNe Ia discovered by the Palomar Transient Factory (PTF; Law et al. 2009; Rau et al. 2009), a project designed to explore the optical transient sky. 82 high-quality spectra of SNe Ia host galaxies were obtained, with precise determinations of their stellar masses, gas-phase and stellar metallicities, stellar ages and SFRs. We then combine these host parameters with optical multicolour light curves of the SNe in an effort to investigate the physical origin of the trends discussed above.

A plan of the paper follows. In Section 2, we introduce the SN Ia sample, and the spectroscopic observations of their host galaxies. Section 3 discusses the various measurements that can be made from these host galaxy spectra, and the methods for measuring SFRs, host galaxy stellar masses, ages and metallicities. In Section 4, we examine how the key SN Ia photometric properties depend on these host parameters, and we discuss our findings in Section 5. We conclude in Section 6. Throughout this paper, we assume $H_0 = 70\,\mathrm{km\,s^{-1}\,mpc^{-1}}$ and a flat universe with $\Omega_M = 0.3$.

2 OBSERVATIONS AND DATA REDUCTION

In this section, we present the sample of SNe Ia and their host galaxies studied in this paper. We discuss the SN sample selection, the observations of the host galaxies and their data reduction, and the photometric light-curve data for the SNe.

2.1 SN sample selection

The SNe Ia studied in this paper were discovered by the PTF, a project which operated from 2009 to 2012 and used the CFH12k wide-field survey camera (Rahmer et al. 2008) mounted on the Samuel Oschin 48 inch telescope (P48) at the Palomar Observatory. The observational cadences used to discover the SNe ranged from hours up to ∼5 d. SN candidates were identified in image subtraction data and ranked using both simple cuts on the detection parameters and a machine learning algorithm (Bloom et al. 2012), and then visually confirmed by members of the PTF collaboration or, from mid-2010 onwards, via the citizen science project 'Galaxy Zoo: Supernova' (Smith et al. 2011). The latter identified eight of the SNe studied in this paper.

Promising SN candidates were then sent for spectroscopic confirmation using a variety of telescope/instrument combinations. These included: The William Herschel Telescope (WHT) and the Intermediate dispersion Spectrograph and Image System (ISIS), the Palomar Observatory Hale 200-in and the double spectrograph, the Keck-I telescope and the Low Resolution Imaging Spectrometer (LRIS), the Keck-II telescope and the DEep Imaging Multi-Object Spectrograph (DEIMOS), the Gemini-N telescope and the Gemini

Multi-Object Spectrograph (GMOS), the Very Large Telescope and X-Shooter, the Lick Observatory 3 m Shane telescope and the Kast Dual Channel Spectrograph, the Kitt Peak National Observatory 4 m telescope and the Richey–Chretien Spectrograph, and the University of Hawaii 88-in and the Supernova Integral Field Spectrograph (SNIFS). All of the spectra used to confirm the SNe in this paper as SN Ia are available from the Weizmann Interactive Supernova data REPository (WISeREP) archive (Yaron & Gal-Yam 2012).

PTF operated in either the R or g' band (hereafter R_{P48} and g_{P48}), switching from g_{P48} band around new moon to R_{P48} band when the sky was brighter. Multicolour light curves were not obtained by default for all SNe using the P48; instead they were assembled via triggered observations on other robotic facilities, e.g., the Liverpool Telescope (LT; Steele et al. 2004), the Palomar 60-in (P60; Cenko et al. 2006) and the Las Cumbres Observatory Global Telescope Network (LCOGT; Brown et al. 2013) Faulkes Telescopes (FTs; clones of the LT).

The full PTF SN Ia sample comprises some 1250 spectroscopically confirmed events. However, many of these are at relatively high redshift and thus have poor quality P48 light curves, or were discovered at the start or end of an observing season and thus have incomplete P48 light curves. In both of these cases no multicolour information is available. Thus, the first task is to define a parent sample of high-quality SNe Ia from which targets for host galaxy studies can be selected. Several criteria were used.

First, the PTF SN Ia programme (generally) restricted multi-colour follow-up to those events with a redshift (z) of $z < 0.09$. The motivation for this was to define a sample less susceptible to selection effects: the median redshift of all PTF SNe Ia is 0.1, and at $z = 0.09$, a typical SN Ia has a peak apparent magnitude of $R_{P48} \simeq 18.5$, $\simeq 2.5$ mag above the PTF detection limit of 21 (a typical SN Ia at $z = 0.09$ has $R_{P48} = 21$ at 13 d before maximum light). We apply the same redshift constraint, giving a parent sample of 527 SNe Ia. Secondly, for this host galaxy study we only considered

SNe Ia with a multicolour light curve: only SNe Ia discovered and confirmed before maximum light were sent for detailed monitoring, with around 220 events followed in this way. Finally, for this paper, we only selected 'older' SNe Ia for study, i.e. those SNe Ia which had already faded by the time the host galaxy spectrum was taken. We took these at >1 year since the SN explosion. This leaves a potential sample of 140 events, all discovered during 2009–2011, which are suitable for our study. Of these events, we had sufficient telescope time to observe 82 host galaxy spectra, selected at random from the parent sample. The host galaxies of the SNe Ia were identified by inspecting images taken by the SDSS. Most of the host galaxies in our sample can be identified unambiguously, except PTF09dav where its likely host galaxy lies ∼41 kpc from the SN (Sullivan et al. 2011a).

A final caveat is that any biases that exist in the selection of the parent PTF sample will also be present in our SN Ia sample. The potentially most serious of these is the difficulty in finding SNe on very bright galaxy backgrounds, where the contrast of the SN over the host galaxy is low. This can occur in the cores of galaxies (e.g. Shaw 1979) but also more generally for faint events in bright host galaxies (e.g. Perrett et al. 2010), which of course are also likely to be the most metal rich. However, with modern image subtraction techniques this is only an issue when the SN brightness drops to <10 per cent of that of the host background (Perrett et al. 2010), and the redshift cuts used in our sample definition mean this is unlikely to occur for normal SNe Ia.

Fig. 1 shows a comparison of the distributions of our host galaxy sample and the various larger PTF samples in redshift, host galaxy r-band apparent magnitude (m_r) and host galaxy stellar mass, $M_{stellar}$ (the determination of $M_{stellar}$ is described in Section 3). The parent PTF sample shown in Fig. 1 contains the 527 $z < 0.09$ PTF SNe Ia, although only 443 of these have Sloan Digital Sky Survey (SDSS) *ugriz* imaging data from which $M_{stellar}$ estimates could be made (Section 2.5). Of the 84 events for which SDSS photometry is
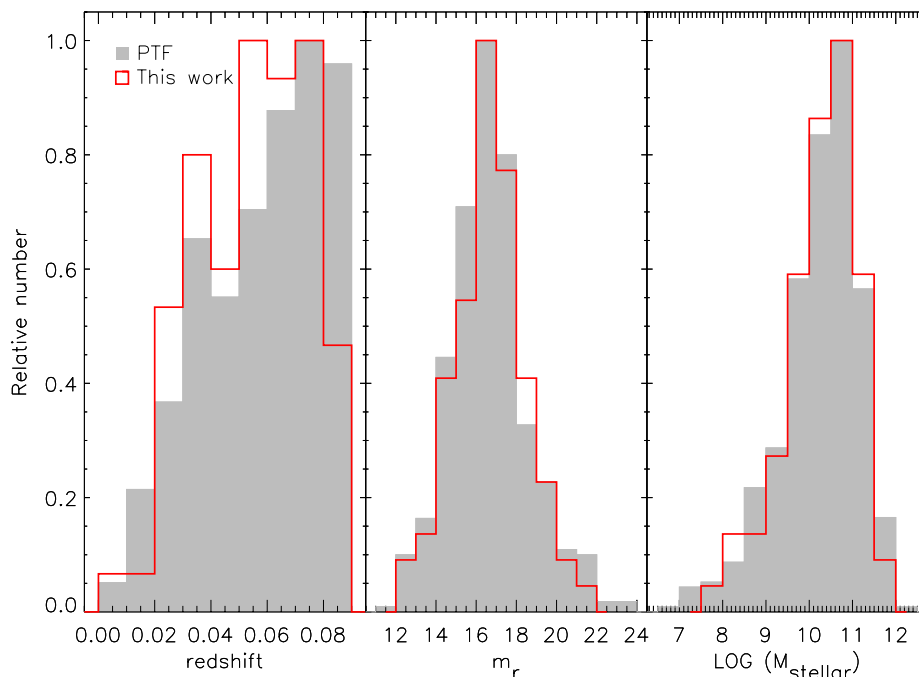

Figure 1. The distribution in SN redshift, SDSS r-band host galaxy apparent magnitude (m_r), and host galaxy stellar mass ($M_{stellar}$) of our 82 PTF SNe Ia host galaxies. The larger PTF SN Ia sample is shown as the filled grey histogram (527 SNe Ia in the redshift histogram, and 443 events in the m_r and $M_{stellar}$ panels), and our host galaxy sample studied as the open red histogram.

Table 1. The instrumental setups used for the spectroscopic data.

Telescope	Spectrograph	Gratings/Grisms		Dichroic	λ coverage
		(Red)	(Blue)		(Å)
Gemini	GMOS	R400	B600	–	3600–9400
WHT	ISIS	R158R	R300B	5336 Å	3000–10000
Lick	Kast	300/7500	600/4310	5500 Å	3000–11000
Keck	LRIS	400/8500	600/4000	5696 Å	3200–10000

not available, 74 lie outside the SDSS footprint, and the remaining 10 SNe Ia have no host galaxy visible in the SDSS images. A K-S test gives a 35, 77 and 99 per cent probability that our host galaxy sample and the larger PTF sample are drawn from the same population in redshift, m_r and $M_{stellar}$. Thus, we find no strong evidence that our SN Ia host galaxy sample is biased with respect to the larger PTF sample.

2.2 Host galaxy observations

All of our host galaxy spectra were obtained using spectrographs operating in long-slit mode on four different facilities. Table 1 sum-

marizes the instruments and setups used for our spectroscopic data, and an observational log of the galaxies studied in this paper can be found in Table 2. Generally, our strategy was to place the slit through both the positions of the SN and the centre of the host galaxy. Thus, we were careful to ensure that the observations were taken at low airmass to avoid losses due to not observing at the parallactic angle. The median airmass of the spectroscopic data in this work is ∼1.15.

Most of our SN Ia host galaxy spectra were taken at the Gemini Observatory during 2010–2012 (59 out of 82 hosts), using both Gemini North and Gemini South. We used GMOS (Hook et al. 2004) with a 3600–9400 Å wavelength coverage provided using two different settings (B600 and R400 gratings). Two exposures in each setting were taken, with a ∼100 pixel shift in wavelength space in order to avoid the gaps between the detectors (the GMOS array is composed of three CCDs). Total integration times were around two hours per source.

18 further SN Ia host spectra were taken at the 4.2 m WHT using ISIS, providing 3000–10 000 Å wavelength coverage. ISIS is a dual-armed spectrograph, and we used the R300B and R158R gratings in the blue and red arms, respectively. The 5300 dichroic was used.

Table 2. The observing log of full sample used in this paper.

SN name	Coordinate		Instrument	Exp. time[a]		Redshift (z)[b]		S/N
	(RA)	(Dec.)		(Blue)	(Red)	(Spec.)	(CMB)	
PTF09dav	22:46:52.95	+21:38:21.5	Gemini+GMOS	3000	3000	0.0371	0.0359	42
PTF09dlc	21:46:30.02	+06:25:07.3	Gemini+GMOS	4000	4000	0.0672	0.0660	15
PTF09dnl	17:23:41.69	+30:29:51.0	Gemini+GMOS	3000	3000	0.0237	0.0236	13
PTF09dnp	15:19:25.34	+49:30:05.0	Gemini+GMOS	3600	3600	0.0370	0.0373	28
PTF09dxo	02:01:47.64	−07:05:34.4	Gemini+GMOS	4000	3000	0.0519	0.0510	35
PTF09dxw	23:44:50.66	+27:37:28.9	Gemini+GMOS	3000	3000	0.0293	0.0282	46
PTF09dza	21:03:31.68	−04:20:35.5	Gemini+GMOS	4000	4000	0.0832	0.0822	44
PTF09edr	00:11:42.89	+30:14:22.6	Gemini+GMOS	3000	3000	0.0857	0.0846	35
PTF09eoi	23:24:12.96	+12:46:46.6	Gemini+GMOS	3000	3000	0.0410	0.0398	39
PTF09fox	23:20:47.79	+32:30:06.1	Gemini+GMOS	3000	3000	0.0718	0.0707	33
PTF09foz	00:42:11.90	−09:52:54.8	Gemini+GMOS	3000	3600	0.0543	0.0532	35
PTF09gce	23:38:49.63	+28:16:13.8	Gemini+GMOS	3000	3000	0.0575	0.0564	30
PTF09gon	22:42:45.53	+05:09:28.8	Gemini+GMOS	4000	3600	0.0680	0.0668	36
PTF09gul	01:28:23.90	+33:51:40.7	Gemini+GMOS	3600	3600	0.0725	0.0716	39
PTF09hpl	01:21:29.18	+00:06:28.8	Gemini+GMOS	4000	3600	0.0781	0.0771	41
PTF09hpq	00:41:12.91	−09:09:00.4	Gemini+GMOS	4000	3600	0.0529	0.0518	34
PTF09hql	01:55:29.30	+13:13:50.9	Gemini+GMOS	3000	3000	0.0499	0.0490	28
PTF09hqp	03:10:30.61	+35:05:02.2	Gemini+GMOS	3000	3000	0.0218	0.0212	37
PTF09ifh	04:10:35.27	+27:23:32.1	Gemini+GMOS	3000	3000	0.0788	0.0784	32
PTF10aaiw	01:09:21.02	+15:44:06.7	Gemini+GMOS	4000	3600	0.0600	0.0589	30
PTF10accd	02:13:30.50	+46:41:38.4	Gemini+GMOS	4000	4000	0.0348	0.0341	27
PTF10acnz	11:44:56.31	+58:39:46.1	Gemini+GMOS	3600	3600	0.0615	0.0620	21
PTF10bxs	10:58:44.28	+32:27:08.3	Gemini+GMOS	3600	3600	0.0727	0.0737	34
PTF10duz	12:51:40.03	+14:26:29.4	Gemini+GMOS	3600	3600	0.0640	0.0650	28
PTF10fps	13:29:24.26	+11:47:49.2	Gemini+GMOS	4000	3600	0.0214	0.0224	32
PTF10fxl	16:52:48.63	+51:03:41.0	Gemini+GMOS	3600	3600	0.0296	0.0295	41
PTF10gmd	11:57:18.96	+57:11:58.6	Gemini+GMOS	3600	3600	0.0552	0.0557	36
PTF10gmg	16:24:58.54	+51:02:22.2	Gemini+GMOS	3600	3600	0.0628	0.0628	28
PTF10hdn	14:52:24.58	+47:28:34.3	Gemini+GMOS	3600	3600	0.0699	0.0703	22
PTF10hdv	12:07:45.43	+41:29:28.7	Keck+LRIS	1800	1800	0.0527	0.0535	5
PTF10hjw	12:52:18.00	−07:01:06.7	Gemini+GMOS	3600	3600	0.0417	0.0428	30
PTF10hml	13:19:50.66	+41:58:57.4	Gemini+GMOS	3600	3600	0.0534	0.0541	15
PTF10icb	12:54:49.78	+58:52:56.6	Gemini+GMOS	2400	2400	0.0085	0.0089	31
PTF10iyc	17:09:22.03	+44:23:30.1	Gemini+GMOS	3600	3600	0.0594	0.0593	32
PTF10jdw	15:41:59.95	+47:35:29.8	Gemini+GMOS	3600	3600	0.0766	0.0768	32
PTF10jtp	17:10:58.51	+39:28:28.9	Gemini+GMOS	3600	3600	0.0670	0.0669	23
PTF10mwb	17:17:50.04	+40:52:52.7	Gemini+GMOS	4000	4000	0.0310	0.0309	11

Table 2 – *continued*

SN name	Coordinate		Instrument	Exp. time[a]		Redshift (z)[b]		S/N
	(RA)	(Dec.)		(Blue)	(Red)	(Spec.)	(CMB)	
PTF10nkd	15:45:21.41	+52:13:50.5	Gemini+GMOS	3600	3600	0.0676	0.0678	31
PTF10nlg	16:50:34.55	+60:16:34.6	Gemini+GMOS	3600	3600	0.0562	0.0561	27
PTF10pvi[c]	22:02:02.42	+14:32:07.1	WHT+ISIS	3600	3600	0.0802	0.0790	12
PTF10qjl	16:39:59.23	+12:06:26.6	WHT+ISIS	1800	1800	0.0576	0.0577	6
PTF10qjq	17:07:12.36	+35:30:35.6	Gemini+GMOS	3600	3600	0.0284	0.0283	24
PTF10qkf	23:14:23.04	+10:45:17.3	WHT+ISIS	3600	3600	0.0804	0.0792	19
PTF10qkv[c]	17:11:52.75	+27:22:20.3	WHT+ISIS	1200	1200	0.0611	0.0610	18
PTF10qky[c]	22:17:49.08	+05:25:23.5	Gemini+GMOS	3600	3600	0.0742	0.0730	38
PTF10qny[c]	16:09:30.67	+22:20:10.0	Gemini+GMOS	4000	4000	0.0333	0.0335	30
PTF10qsc	21:34:21.12	−05:03:46.1	WHT+ISIS	3600	3600	0.0879	0.0868	8
PTF10qwg	02:42:09.96	+02:26:51.0	Gemini+GMOS	4000	3600	0.0679	0.0671	37
PTF10rab[c]	01:47:07.46	−00:02:58.9	Keck+LRIS	1800	1800	0.0850	0.0840	5
PTF10rbp[c]	01:16:37.78	−01:49:28.2	Gemini+GMOS	4000	4000	0.0823	0.0813	38
PTF10tce	23:19:09.74	+09:11:45.6	WHT+ISIS	5400	5400	0.0410	0.0398	10
PTF10trp	21:28:08.01	+09:51:14.0	Gemini+GMOS	4000	4000	0.0489	0.0478	27
PTF10twd	23:00:14.23	+20:47:59.3	Gemini+GMOS	4000	4000	0.0734	0.0722	25
PTF10ubm	00:01:59.23	+21:49:31.1	Gemini+GMOS	3600	3600	0.0701	0.0689	27
PTF10viq	22:20:19.46	+17:03:25.2	WHT+ISIS	1800	1800	0.0342	0.0330	33
PTF10wnm	00:22:03.70	+27:02:21.5	WHT+ISIS	2400	2400	0.0663	0.0652	18
PTF10wnq	00:49:10.10	+32:08:14.3	WHT+ISIS	2400	2400	0.0691	0.0681	19
PTF10wof[c]	23:32:41.42	+15:21:31.7	WHT+ISIS	3000	3000	0.0530	0.0518	13
PTF10wor	22:32:41.67	−09:27:46.8	Gemini+GMOS	4000	3600	0.0568	0.0556	31
PTF10trp	21:28:08.01	+09:51:14.0	Gemini+GMOS	4000	4000	0.0489	0.0478	27
PTF10twd	23:00:14.23	+20:47:59.3	Gemini+GMOS	4000	4000	0.0734	0.0722	25
PTF10ubm	00:01:59.23	+21:49:31.1	Gemini+GMOS	3600	3600	0.0701	0.0689	27
PTF10viq	22:20:19.46	+17:03:25.2	WHT+ISIS	1800	1800	0.0342	0.0330	33
PTF10wnm	00:22:03.70	+27:02:21.5	WHT+ISIS	2400	2400	0.0663	0.0652	18
PTF10wnq	00:49:10.10	+32:08:14.3	WHT+ISIS	2400	2400	0.0691	0.0681	19
PTF10wof[c]	23:32:41.42	+15:21:31.7	WHT+ISIS	3000	3000	0.0530	0.0518	13
PTF10wor	22:32:41.67	−09:27:46.8	Gemini+GMOS	4000	3600	0.0568	0.0556	31
PTF10wos	21:44:39.36	−05:25:22.4	Gemini+GMOS	4000	4000	0.0820	0.0809	38
PTF10xyt	23:19:02.43	+13:47:26.2	Gemini+GMOS	3600	3600	0.0490	0.0478	37
PTF10yer	21:29:01.37	−01:25:51.6	Gemini+GMOS	4000	4000	0.0528	0.0517	53
PTF10ygu[c]	09:37:29.83	+23:09:41.8	Lick+KAST	600	600	0.0259	0.0269	14
PTF10yux	23:24:13.92	+07:13:39.7	Gemini+GMOS	3600	3600	0.0578	0.0566	38
PTF10zbk	02:29:34.46	+22:20:00.2	Gemini+GMOS	4000	4000	0.0642	0.0634	30
PTF10zdk	02:14:07.37	+23:37:49.1	WHT+ISIS	2400	2400	0.0322	0.0314	13
PTF10zgy	02:38:43.77	+14:06:11.9	Gemini+GMOS	4000	4000	0.0443	0.0435	25
PTF11apk	10:21:00.53	+21:42:59.8	Gemini+GMOS	3600	3600	0.0405	0.0416	28
PTF11atu	15:31:14.91	−00:46:45.8	Gemini+GMOS	4000	4000	0.0774	0.0779	23
PTF11bas	13:16:47.78	+43:31:13.4	Lick+KAST	2400	2400	0.0863	0.0870	15
PTF11bju	11:56:14.40	+25:21:14.8	Gemini+GMOS	4000	4000	0.0323	0.0333	31
PTF11htb	21:55:37.01	+00:41:29.4	WHT+ISIS	5400	5400	0.0493	0.0481	9
PTF11khk	17:02:58.03	+40:31:28.6	WHT+ISIS	3600	3600	0.0306	0.0305	26
PTF11kjn	22:45:03.93	+33:59:46.0	WHT+ISIS	3600	3600	0.0234	0.0223	29
PTF11kx	08:09:13.20	+46:18:42.8	Gemini+GMOS	4000	4000	0.0467	0.0472	39
PTF11lih	23:10:58.93	+31:51:36.0	WHT+ISIS	3600	3600	0.0720	0.0709	19
PTF11mty	21:34:05.21	+10:25:24.6	WHT+ISIS	3600	3600	0.0770	0.0759	20
PTF11okh	23:06:04.85	+34:06:27.7	WHT+ISIS	3600	3600	0.0191	0.0180	26
PTF11opu	22:07:50.02	+27:47:47.0	WHT+ISIS	3600	3600	0.0649	0.0638	9
PTF11pfm	21:44:13.80	+00:56:34.1	Keck+LRIS	1800	1800	0.0795	0.0784	8
PTF11v	15:08:23.42	+49:39:57.6	Gemini+GMOS	2400	2400	0.0373	0.0376	29
PTF11vl	16:28:40.27	+27:43:39.7	Gemini+GMOS	4000	4000	0.0454	0.0455	28

[a]The exposure time for red or blue gratings/grisms in unit of second.
[b]Here we demonstrate two redshifts based on heliocentric or CMB frame.
[c]'Galaxy Zoo Supernovae project' discovered SNe.

Two brighter host galaxy spectra were taken with the 3 m Shane telescope at the Lick Observatory, using the Kast Spectrograph (Miller & Stone 1993) providing 3000–11 000 Å wavelength coverage. Here, the 300/7500 grating was used for the red arm and 600/4310 grism for the blue arm, using the D55 dichroic.

Finally the 10 m telescope Keck-I telescope was used to observe three fainter ($m_r \geq 20$) host galaxies using LRIS (Oke et al. 1995) with a 3200–10 000 Å wavelength coverage. LRIS is also a dual-armed spectrograph. The 400/8500 grating was used for the red arm and the 600/4000 grism for the blue arm, with the D560 dichroic.
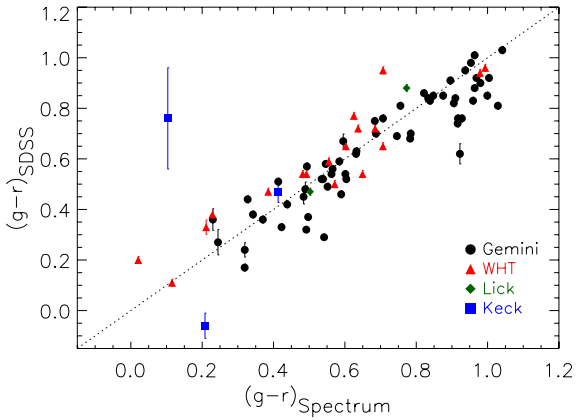
Figure 2. The $g - r$ colour derived from our host galaxy spectra, compared with that determined from the SDSS broad-band photometry. The line of equality is shown in dotted line.

2.3 Spectral data reduction

We reduced our data using a custom data reduction pipeline written in IRAF.[1] For data taken at the Gemini Observatory, we also used some tasks from the Gemini IRAF package. Our pipeline follows standard procedures, including bias subtraction, flat-fielding, cosmic ray removal (using LACOSMIC; van Dokkum 2001) and a wavelength calibration. The IRAF task APALL is then used to extract the 1D spectrum from each 2D frame, and a (relative) flux calibration performed with a telluric-correction by comparing to standard stars. 'Error' spectra are derived from a knowledge of the CCD properties and Poisson statistics, and are tracked throughout the reduction procedure. As all the spectra in our sample are taken either with a spectrograph with two different grating settings (Gemini), or with dual-arm spectrographs with a dichroic (WHT, Lick, Keck), red and blue spectra for each object, with different wavelength coverages and dispersions, need to be combined to produce the final spectrum. This was performed by rebinning to a common dispersion, and combining (with weighting) to form a final contiguous spectrum.

We test our relative flux calibration by comparing synthetic photometry measured from our final host spectra, with SDSS Data Release 9 (DR9; Ahn et al. 2012) photometry of the same objects. The SDSS model magnitudes are used here. Fig. 2 shows the $g - r$ colour of our spectra plotted against the $g - r$ colour from the SDSS photometry. Overall our data show a good consistency with the SDSS photometry: the rms scatter is 0.12 mag, with a mean offset of 0.01 mag.

We correct our absolute flux calibration using the same SDSS photometry (this is important for host galaxy parameters measured based on absolute line strength, for example SFRs). Again, we measure a synthetic SDSS r-band magnitude for our observed spectra, and compare to the SDSS photometry, scaling our observed spectra so the two magnitudes are equal.

Finally, we apply a correction for foreground galactic extinction prior to de-redshifting the spectra into the rest-frame. The latest calibration (Schlafly & Finkbeiner 2011) is used, and the typical

Milky Way value $R_V = 3.1$ is assumed, using a Cardelli, Clayton & Mathis (1989, CCM) law. Although redshift estimates based on the original SN classification spectrum are available, we confirm these using emission and absorption lines in the galaxy spectra; the two redshift measures are consistent in all cases.

The quality of our spectra is quite diverse. We estimate the signal-to-noise ratio (S/N) over a region in the centre of each spectrum ($\sim$5500–6000 Å). The median flux and standard deviation within that region are measured, and the S/N taken as the ratio of the two. Our spectra have a S/N ranging from 5 to 53 with a median of $\simeq$28.

2.4 SN photometry and light-curve fitting

Optical light curves of our SNe Ia in *gri* were obtained at the LT, the P60 and the FTs. There are 66 events with available LT (54 events), P60 (6 events) or FT (6 events) light curves, complemented by P48 R_{P48} (and sometimes g_{P48}) light curves from the rolling PTF search. In all cases, reference images were made by stacking data taken >1 year after the SN explosion, which was then subtracted from the images containing SN light to remove the host galaxy. We measure the SN photometry using a point spread function (PSF) fitting method. In each image frame, the PSF is determined from nearby field stars, and this average PSF is then fit at the position of the SN event weighting each pixel according to Poisson statistics, yielding an SN flux and flux error.

The SIFTO light-curve fitting code (Conley et al. 2008) was used to fit the light curves. SIFTO works in flux space, manipulating a model of the spectral energy distribution (SED) and synthesizing an observer-frame light curve from a given spectral time series in a set of filters at a given redshift, allowing an arbitrary normalization in each observed filter (i.e. the absolute colours of the template being fit are not important and do not influence the fit). The time-axis of the template is adjusted by a dimensionless relative 'stretch' (s) factor to fit the data, where the input template is defined to have $s = 1$. Once the observer-frame SIFTO fit is complete, a second step can be used to estimate rest-frame magnitudes in any given set of filters, provided there is equivalent observer-frame filter coverage, and at any epoch. This is performed by adjusting the template SED at the required epoch to have the correct observed colours from the SIFTO fit, correcting for extinction along the line of sight in the Milky Way, de-redshifting, and integrating the resultant SED through the required filters. This process is essentially a cross-filter *k*-correction, with the advantage that all the observed data contribute to the SED shape used.

We used SIFTO to determine the time of maximum light in the rest-frame *B*-band, the stretch, the rest-frame *B*-band apparent magnitude at maximum light m_B and the $B - V$ colour at *B*-band maximum light, $\mathcal{C}$. When estimating the final SN colour via the template SED adjustment, filters that are very close in effective wavelength can introduce discontinuities in the adjusted spectrum. Thus, we remove the P48 R_{P48} and g_{P48} filters in this process where data from the LT, P60 or FTs are also available. Note that the P48 filters are always used to estimate the stretch and time of maximum light. Fig. 3 shows the distribution of our SNe Ia in stretch and colour. As a comparison, we overplot the higher redshift Supernova Legacy Survey (SNLS) sample studied by Guy et al. (2010) for SNLS events at $z < 0.6$ where the SNLS sample is more complete (Perrett et al. 2010). We generally find good agreement in the stretch and colour distributions, although our sample probes faster (lower stretch) and redder SNe Ia than SNLS. A complete list of the SN photometric measurements can be found in Table 3.

---

[1] The Image Reduction and Analysis Facility (IRAF) is distributed by the National Optical Astronomy Observatories, which are operated by the Association of Universities for Research in Astronomy, Inc., under cooperative agreement with the National Science Foundation.
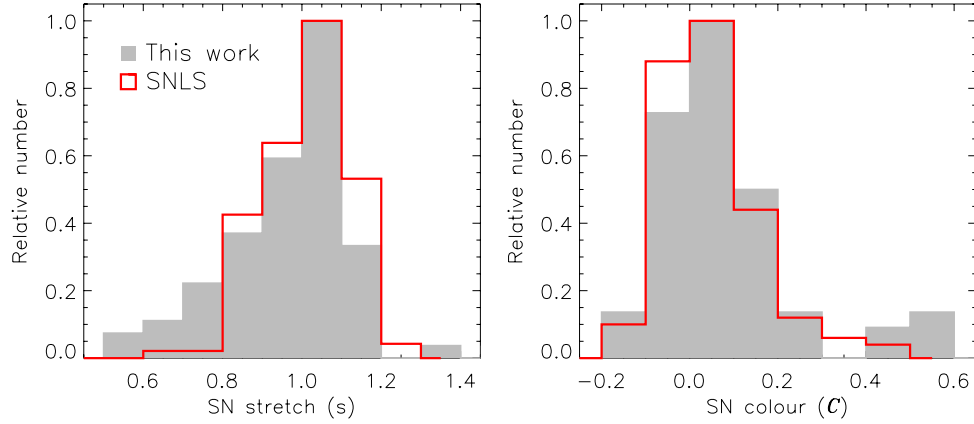
Figure 3. The grey filled histograms show the SN stretch (s) and colour ($\mathcal{C}$) distributions of our PTF sample (see Section 2.4 for more details). The SNLS sample of Guy et al. (2010) at $z < 0.6$ is overplotted in the red open histogram.

Table 3. The SN photometric properties in this paper.

| | | SN photometric properties[a] | | |
SN name	LC source[b]	Stretch (s)	Colour ($\mathcal{C}$)	m_B (mag)
PTF09dav	P48	0.64 ± 0.04	–	–
PTF09dlc	P48; FT	1.06 ± 0.01	0.02 ± 0.01	18.17 ± 0.02
PTF09dnl	P48; LT	1.05 ± 0.02	− 0.02 ± 0.01	15.85 ± 0.02
PTF09dnp	P48; FT	0.98 ± 0.03	0.11 ± 0.02	17.09 ± 0.02
PTF09dxo	P48	1.08 ± 0.04	–	–
PTF09dxw	P48	0.72 ± 0.05	–	–
PTF09dza	P48	–	–	–
PTF09edr	P48	0.81 ± 0.11	–	–
PTF09eoi	P48	–	–	–
PTF09fox	P48; LT	0.95 ± 0.04	0.03 ± 0.04	18.34 ± 0.06
PTF09foz	P48; LT	0.85 ± 0.04	0.00 ± 0.06	17.78 ± 0.09
PTF09gce	P48; P60	1.06 ± 0.05	− 0.03 ± 0.03	17.70 ± 0.07
PTF09gon	P48	–	–	–
PTF09gul	P48	0.89 ± 0.06	–	–
PTF09hpl	P48	0.89 ± 0.05	–	–
PTF09hpq	P48	0.82 ± 0.08	–	–
PTF09hql	P48	1.11 ± 0.04	–	–
PTF09hqp	P48	1.16 ± 0.03	–	–
PTF09ifh	P48	–	–	–
PTF10aaiw	–	–	–	–
PTF10accd	P48; LT	1.03 ± 0.02	− 0.11 ± 0.02	16.60 ± 0.05
PTF10acnz	P48; FT	1.10 ± 0.01	0.10 ± 0.01	17.98 ± 0.01
PTF10bxs	P48; P60	1.08 ± 0.05	0.11 ± 0.09	18.81 ± 0.12
PTF10duz	P48; P60	0.97 ± 0.03	− 0.01 ± 0.02	18.06 ± 0.03
PTF10fps	P48; LT	0.72 ± 0.02	0.12 ± 0.03	16.66 ± 0.05
PTF10fxl	P48; FT	0.97 ± 0.02	0.10 ± 0.01	16.76 ± 0.02
PTF10gmd	P48; FT	0.78 ± 0.01	0.09 ± 0.01	18.35 ± 0.02
PTF10gmg	P48; P60	1.11 ± 0.02	− 0.03 ± 0.02	17.91 ± 0.03
PTF10hdn	P48; LT	1.09 ± 0.03	–	–
PTF10hdv	P48; FT	1.09 ± 0.01	− 0.03 ± 0.01	17.56 ± 0.01
PTF10hjw	P48; LT	0.99 ± 0.02	− 0.09 ± 0.04	16.99 ± 0.06
PTF10hml	P48; LT	1.02 ± 0.01	− 0.05 ± 0.03	17.71 ± 0.03
PTF10icb	P48; LT	0.98 ± 0.03	0.06 ± 0.02	14.49 ± 0.03
PTF10iyc	P48; LT	1.06 ± 0.02	− 0.03 ± 0.01	17.74 ± 0.01
PTF10jdw	P48; LT	0.84 ± 0.02	–	–
PTF10jtp	P48; LT	0.87 ± 0.01	0.11 ± 0.02	18.69 ± 0.03
PTF10mwb	P48; LT	0.92 ± 0.02	0.03 ± 0.03	16.82 ± 0.04
PTF10nkd	P48; LT	0.92 ± 0.03	–	–
PTF10nlg	P48; LT	0.98 ± 0.03	0.10 ± 0.03	18.59 ± 0.03
PTF10pvi	P48; LT	1.03 ± 0.02	− 0.08 ± 0.02	18.43 ± 0.03
PTF10qjl	P48; LT	0.96 ± 0.02	− 0.11 ± 0.02	17.82 ± 0.02
PTF10qjq	P48; LT	0.93 ± 0.02	0.00 ± 0.02	16.42 ± 0.03
PTF10qkf	P48; LT	1.03 ± 0.02	0.10 ± 0.03	18.95 ± 0.03

Table 3 – *continued*

SN name	LC source[b]	Stretch (s)	Colour ($\mathcal{C}$)	m_B (mag)
		SN photometric properties[a]		
PTF10qkv	P48; LT	1.07 ± 0.04	0.17 ± 0.03	19.15 ± 0.03
PTF10qky	P48; LT	1.07 ± 0.02	-0.06 ± 0.02	18.14 ± 0.04
PTF10qny	P48; P60	1.10 ± 0.07	-0.02 ± 0.02	16.37 ± 0.05
PTF10qsc	P48; LT	1.15 ± 0.02	-0.07 ± 0.02	18.54 ± 0.02
PTF10qwg	P48; LT	0.93 ± 0.04	0.16 ± 0.07	18.58 ± 0.10
PTF10rab	P48; LT	1.06 ± 0.04	–	–
PTF10rbp	P48; LT	1.08 ± 0.03	0.09 ± 0.02	18.76 ± 0.03
PTF10tce	P48; LT	1.08 ± 0.02	0.05 ± 0.02	17.19 ± 0.03
PTF10trp	P48; LT	1.12 ± 0.02	0.59 ± 0.02	19.15 ± 0.03
PTF10twd	P48; LT	1.08 ± 0.02	-0.07 ± 0.01	18.08 ± 0.03
PTF10ubm	P48; LT	1.06 ± 0.01	0.01 ± 0.01	17.98 ± 0.02
PTF10viq	P48; LT	1.13 ± 0.01	0.05 ± 0.02	16.62 ± 0.03
PTF10wnm	P48; LT	1.04 ± 0.02	0.03 ± 0.01	18.20 ± 0.02
PTF10wnq	P48; LT	0.93 ± 0.02	-0.16 ± 0.02	18.10 ± 0.03
PTF10wof	P48; LT	0.99 ± 0.03	0.09 ± 0.04	17.95 ± 0.07
PTF10wor	P48; LT	0.68 ± 0.03	0.55 ± 0.05	20.03 ± 0.11
PTF10wos	P48; LT	0.93 ± 0.05	-0.04 ± 0.02	18.73 ± 0.04
PTF10xyt	P48; LT	1.08 ± 0.03	0.22 ± 0.03	18.44 ± 0.04
PTF10yer	P48; P60	–	–	–
PTF10ygu	P48; LT	1.01 ± 0.02	0.44 ± 0.03	17.27 ± 0.04
PTF10yux	P48; LT	0.84 ± 0.01	0.17 ± 0.02	18.52 ± 0.04
PTF10zbk	P48; LT	0.78 ± 0.03	0.11 ± 0.06	19.28 ± 0.11
PTF10zdk	P48; LT	1.14 ± 0.01	0.06 ± 0.02	16.96 ± 0.04
PTF10zgy	P48; LT	1.16 ± 0.04	0.15 ± 0.03	18.00 ± 0.06
PTF11apk	P48; LT	0.75 ± 0.04	0.21 ± 0.04	18.32 ± 0.05
PTF11atu	P48; LT	0.81 ± 0.04	-0.06 ± 0.04	18.62 ± 0.10
PTF11bas	P48; LT	0.96 ± 0.02	0.06 ± 0.01	18.92 ± 0.02
PTF11bju	P48; LT	1.15 ± 0.01	0.02 ± 0.01	16.62 ± 0.01
PTF11htb	P48; LT	1.06 ± 0.02	0.01 ± 0.02	17.37 ± 0.04
PTF11khk	P48; LT	0.59 ± 0.02	0.41 ± 0.04	17.97 ± 0.06
PTF11kjn	P48; LT	0.62 ± 0.01	0.28 ± 0.02	17.31 ± 0.03
PTF11kx	P48	1.04 ± 0.02	–	–
PTF11lih	P48; LT	0.89 ± 0.01	0.10 ± 0.02	18.97 ± 0.03
PTF11mty	P48; LT	1.05 ± 0.03	0.03 ± 0.03	18.44 ± 0.04
PTF11okh	P48; LT	0.53 ± 0.01	0.56 ± 0.03	18.17 ± 0.06
PTF11opu	P48; LT	1.34 ± 0.03	0.02 ± 0.03	19.39 ± 0.05
PTF11pfm	P48;	–	–	–
PTF11v	P48; LT	0.78 ± 0.01	-0.00 ± 0.03	17.05 ± 0.04
PTF11vl	P48; LT	–	–	–

[a]The SN properties derived by SIFTO light-curve fitting code.
[b]See Section 2.1 for more information.

2.5 Host galaxy photometry

In later sections, we will use broad-band photometry of the SN Ia host galaxies to estimate the host galaxy stellar mass. Where available we use SDSS *ugriz* photometry, but some (five) of our SNe with host galaxy spectra lie outside the SDSS footprint. For these we instead use the LT $g'r'i'$ images taken as part of the SN photometric follow-up campaign, calibrated using observations of either Smith et al. (2002) standard stars, or of the SDSS stripe 82 (Ivezić et al. 2007). The host photometry is measured by SEXTRACTOR (Bertin & Arnouts 1996), which we use in dual-image mode with FLUX_AUTO photometry, ensuring the same consistent aperture is used in each filter.

3 HOST GALAXY PARAMETER DETERMINATION

Having described the sample and data that make up our host galaxy sample, we now discuss the techniques used to fit the SN Ia host galaxy spectra, and estimate various physical parameters such as the SFR and the gas-phase metallicity. We use various techniques, including emission line measurements to determine SFRs and gas-phase metallicities, spectral fitting to determine stellar metallicities and ages, and broad-band photometric fitting to determine stellar masses. We first introduce the technique used to make the emission line measurements.

3.1 Emission line measurement

The emission lines and stellar continuum of the host galaxy spectra are fit using the Interactive Data Language (IDL) codes PPXF (Cappellari & Emsellem 2004) and GANDALF (Sarzi et al. 2006). PPXF fits the line-of-sight velocity distribution (LOSVD) of the stars in the galaxy in pixel space using a series of stellar templates. The advantage of working in pixel space is that emission lines and bad pixels are easily excluded when fitting the continuum. Before fitting the stellar continuum, a list of emission lines is used to mask

this potential contamination. The stellar templates are based on the MILES empirical stellar library (Sánchez-Blázquez et al. 2006; Vazdekis et al. 2010), giving a wavelength coverage of 3540 Å to 7410 Å with a spectral resolution of 2.51 Å, and a variety of different metallicities and ages. A total of 276 templates are selected with [M/H] = −1.71 to +0.22 in six steps and ages ranging from 0.079 to 14.12 Gyr in 46 steps.

After measuring the stellar kinematics with PPXF, the emission lines and stellar continuum are simultaneously fit by GANDALF. GANDALF treats the emission lines as additional Gaussian templates. Through an iterative fitting process, GANDALF locates the best velocities and velocity dispersions of each Gaussian template and also the optimal combination of the stellar templates which have already been convolved with the LOSVD. This results in the emission lines and stellar continuum being fit simultaneously to each spectrum.

Extinction is handled using a two-component reddening model. The first component assumes a diffusive dust throughout the whole galaxy that affects the entire spectrum including emission lines and the stellar continuum, while the second is a local dust component around the nebular regions, and therefore affects only the emission lines. The first component is determined by comparing the observed spectra to the un-reddened spectral templates. However, the local dust component is constrained only if the Balmer decrement (the Hα $\lambda 6563$ to Hβ $\lambda 4861$ line ratio) can be measured. For galaxies without Balmer lines in their spectra, only the diffusive dust component is fit (26 out of 82 hosts). To ensure the emission lines in our spectrum are well measured, we required an S/N > 3 (S/N is defined as the ratio of line amplitude to the noise of the spectrum) for emission lines used in the determination of host parameters.

3.2 AGN contamination

Our next task is to check for active galactic nuclei (AGN) activity in our host galaxies. In galaxies hosting an AGN, non-thermal emission from the AGN can dominate over that from the hot stars, leading to a different ionization source for the nebular H II regions. This in turn means that the emission line measurements performed in the previous section cannot be interpreted using the techniques discussed later in this section.

We adopt the BPT diagram (Baldwin, Phillips & Terlevich 1981), shown in Fig. 4 for our sample. The galaxies are divided into two groups using either the criteria proposed by Kewley et al. (2001) or Kauffmann et al. (2003). Any galaxies lying to the right of these lines in Fig. 4 are regarded as potential AGN host galaxies. We adopt the Kewley et al. criterion: a galaxy will be identified as an AGN if

$$\log\left([O\,\textsc{iii}]/H\beta\right) > \frac{0.61}{\log\left([N\,\textsc{ii}]/H\alpha\right) - 0.47} + 1.19, \qquad (1)$$

where N II is the flux of $\lambda 6584$ line, and O III the $\lambda 4959$, 5007 lines. However, this requires the four emission lines to be well detected. For those spectra with only O III and Hβ or N II and Hα available, 'two-line' methods can be used (Miller et al. 2003): a galaxy will be identified as an AGN if

$$\log\left([N\,\textsc{ii}]/H\alpha\right) > -0.2 \qquad (2)$$

or

$$\log\left([O\,\textsc{iii}]/H\beta\right) > 0.8. \qquad (3)$$

Note that these two-line criteria are more conservative than Kewley et al. criterion. There are 11 (3 by the two-line methods) galaxies
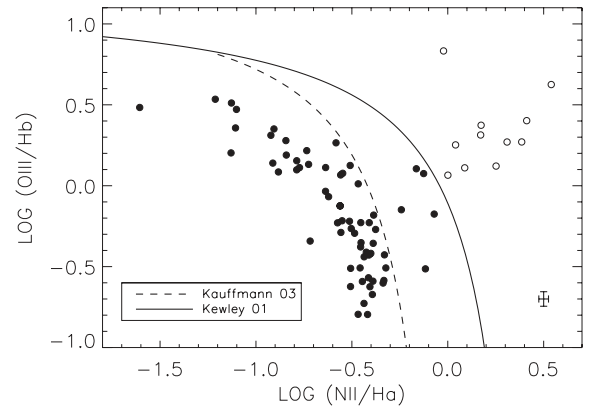

Figure 4. The BPT diagram used to identify the AGN host galaxies in our sample. Two different criteria are overplotted: Kewley et al. (2001) and Kauffmann et al. (2003). The galaxies which lie on the right-hand side of Kewley 01 criteria will be regarded as potential AGN host galaxies in this work (the open circles). Normal star-forming galaxies are plotted in filled circles. The representative error is shown in the bottom-right corner.

in our sample identified as AGN, and these are discarded from the sample for further emission line analyses. A further five galaxies would have been excluded based on the Kauffmann et al. criterion. We have checked that including these objects does not affect our results.

3.3 Determination of host parameters

Having measured the emission lines of the SN hosts, and removed galaxies likely hosting AGN from our sample, we now turn to the estimation of various host galaxy physical properties: the host galaxy SFR, the gas-phase metallicity, the mean stellar metallicity and age, and the stellar mass. A complete list of the host parameters measured in this section can be found in Tables 4 and 5.

3.3.1 Star formation rate

The SFR of a galaxy can be estimated using nebular lines in the spectrum, with Hα the most popular choice due to its intrinsic strength and location in the redder part of the spectrum, leading to a lower susceptibility to dust extinction. As this emission line is produced from ionizing photons generated by the most massive, youngest stars, the SFR estimated is a nearly instantaneous measure. We adopt the conversion of Kennicutt (1998), which used evolutionary synthesis models to relate the luminosity of the Hα line, $L(H\alpha)$, to the SFR via

$$SFR = 7.9 \times 10^{-42} \times L(H\alpha)\ M_\odot\ yr^{-1} \qquad (4)$$

with $L(H\alpha)$ measured in erg s^{-1}. The relation assumes case B recombination and a Salpeter (1955) initial mass function (IMF). Brinchmann et al. (2004) studied the likelihood distribution of the conversion factor between $L(H\alpha)$ and SFR, and found a ~0.4 dex variation between high-mass and low-mass galaxies, with the Kennicutt (1998) conversion factor close to the median value of their study. As a result, and following D'Andrea et al. (2011), we adopt a 0.2 dex uncertainty in our SFR measurements.

Table 4. The host photometric properties in this paper.

SN name	$M_{stellar}-$	$M_{stellar}$ ($M_\odot$)	$M_{stellar}+$	logSFR$-$	logSFR ($M_\odot$ yr^{-1})	logSFR$+$
					Host photometric properties[a]	
PTF09dav	10.20	10.28	10.46	0.47	0.58	0.65
PTF09dlc	8.93	8.94	9.09	$-$0.67	$-$0.62	$-$0.60
PTF09dnl	7.98	8.06	8.39	–	–	$-$0.76
PTF09dnp	10.55	10.71	10.73	–	–	–
PTF09dxo	10.20	10.72	10.80	–	$-$0.38	$-$0.36
PTF09dxw	9.45	9.48	9.67	$-$0.36	$-$0.21	$-$0.21
PTF09dza	10.27	10.43	10.56	0.19	0.50	0.60
PTF09edr	11.27	11.30	11.41	–	–	0.18
PTF09eoi	9.24	9.39	9.47	–	–	–
PTF09fox	10.27	10.36	10.43	0.43	0.47	0.56
PTF09foz	10.40	10.56	10.56	–	–	–
PTF09gce	10.82	10.86	10.95	–	$-$0.28	0.40
PTF09gon	11.22	11.23	11.34	–	–	–
PTF09gul	10.99	11.11	11.14	–	$-$0.32	$-$0.04
PTF09hpl	10.62	10.69	10.87	0.91	1.03	1.08
PTF09hpq	10.38	10.38	10.42	–	–	–
PTF09hql	9.40	9.50	9.61	$-$0.32	$-$0.25	$-$0.15
PTF09hqp	–	10.90	–	–	0.96	–
PTF09ifh	–	10.80	–	–	0.58	–
PTF10aaiw	10.64	10.66	10.76	–	$-$0.44	0.04
PTF10accd	9.05	9.13	9.51	–	–	$-$0.28
PTF10acnz	10.63	10.64	10.67	–	–	–
PTF10bxs	10.62	10.72	10.91	0.39	0.90	0.95
PTF10duz	10.15	10.18	10.25	0.56	0.61	0.62
PTF10fps	10.39	10.49	10.51	–	–	–
PTF10fxl	10.53	11.08	11.17	–	$-$0.02	0.49
PTF10gmd	10.30	10.36	10.38	–	–	–
PTF10gmg	9.67	9.77	9.80	0.05	0.07	0.13
PTF10hdn	8.65	8.79	8.95	$-$0.28	$-$0.13	0.05
PTF10hdv	7.51	7.72	7.97	$-$1.43	$-$1.21	$-$0.94
PTF10hjw	–	10.00	–	–	0.43	–
PTF10hml	9.83	9.95	10.38	–	–	1.06
PTF10icb	9.54	9.60	9.75	$-$0.15	$-$0.05	$-$0.02
PTF10iyc	10.52	10.56	11.20	–	–	1.25
PTF10jdw	10.81	10.90	11.11	0.51	1.12	1.17
PTF10jtp	11.13	11.14	11.24	$-$0.06	0.09	0.76
PTF10mwb	8.98	9.31	9.55	–	$-$0.37	$-$0.29
PTF10nkd	9.63	9.70	9.85	$-$0.04	0.03	0.09
PTF10nlg	–	10.01	–	–	0.45	–
PTF10pvi	10.17	10.31	10.45	0.48	0.54	0.65
PTF10qjl	8.00	8.46	8.67	$-$0.96	$-$0.48	$-$0.25
PTF10qjq	9.49	9.56	9.62	0.57	0.65	0.71
PTF10qkf	10.37	10.40	10.50	0.50	0.58	0.63
PTF10qkv	10.43	10.50	10.61	$-$0.11	0.59	0.66
PTF10qky	10.46	10.53	10.69	0.75	0.86	0.92
PTF10qny	10.17	10.69	10.81	–	$-$0.40	0.48
PTF10qsc	9.77	9.83	9.90	0.17	0.18	0.25
PTF10qwg	9.91	10.00	10.22	$-$0.19	0.23	0.27
PTF10rab	7.14	8.15	8.87	–	–	$-$0.63
PTF10rbp	10.70	11.16	11.25	–	0.73	1.29
PTF10tce	10.38	10.51	10.69	0.62	0.73	0.81
PTF10trp	10.14	10.27	10.40	0.41	0.47	0.58
PTF10twd	9.86	10.00	10.05	0.21	0.23	0.31
PTF10ubm	10.00	10.11	10.17	0.37	0.39	0.48
PTF10viq	10.81	10.94	10.99	0.18	0.26	1.04
PTF10wnm	10.52	10.56	10.59	0.70	0.71	0.75
PTF10wnq	11.29	11.36	11.42	–	–	–
PTF10wof	9.93	10.09	10.19	0.19	0.25	0.37
PTF10wor	11.45	11.51	11.57	–	–	–
PTF10wos	11.23	11.25	11.30	0.07	0.16	0.20
PTF10xyt	9.49	9.69	9.79	$-$0.25	$-$0.24	$-$0.06
PTF10yer	10.58	10.66	10.87	0.76	0.91	0.95

Table 4 – *continued*

SN name	$M_{stellar}-$	$M_{stellar}$ (M$_\odot$)	$M_{stellar}+$	logSFR$-$	logSFR (M$_\odot$ yr^{-1})	logSFR$+$
			Host photometric properties[a]			
PTF10ygu	10.70	11.40	11.44	–	–	0.14
PTF10yux	11.23	11.29	11.33	–	–	–
PTF10zbk	10.71	10.80	10.85	-0.64	0.17	0.80
PTF10zdk	9.08	9.15	9.64	0.02	0.23	0.29
PTF10zgy	–	11.39	–	–	1.38	–
PTF11apk	10.74	10.90	10.91	–	–	–
PTF11atu	9.39	9.77	9.99	–	-0.13	-0.01
PTF11bas	9.71	9.75	9.80	0.12	0.16	0.18
PTF11bju	9.51	9.58	9.61	-0.16	-0.14	-0.08
PTF11htb	8.94	8.99	9.02	-0.72	-0.71	-0.66
PTF11khk	10.53	10.70	10.74	–	–	–
PTF11kjn	11.56	11.62	11.67	–	–	–
PTF11kx	10.20	10.26	10.48	0.42	0.59	0.60
PTF11lih	10.64	10.70	10.86	0.85	0.96	0.99
PTF11mty	9.86	9.93	10.08	0.24	0.32	0.34
PTF11okh	11.35	11.40	11.45	–	–	0.03
PTF11opu	9.74	9.82	9.97	0.05	0.12	0.21
PTF11pfm	8.98	9.12	9.20	-0.68	-0.66	-0.57
PTF11v	11.05	11.06	11.23	–	–	–
PTF11vl	9.64	10.07	10.30	–	0.29	0.42

[a]The host parameters determined photometrically by Z-PEG.

Table 5. The host spectroscopic properties in this paper.

SN name	12+log(O/H)	logSFR (M$_\odot$ yr^{-1})	[M/H]	logAge (Gyr)	AGN[b]
		Host spectroscopic properties[a]			
PTF09dav	8.698 ± 0.073	0.0778 ± 0.2001	-0.476	0.406	0
PTF09dlc	8.182 ± 0.069	-0.7730 ± 0.2002	-1.106	0.832	0
PTF09dnl	–	-2.0440 ± 0.2003	-1.107	0.808	0
PTF09dnp	8.758 ± 0.081	<-1.5310	-0.130	1.110	1
PTF09dxo	8.732 ± 0.075	-0.1270 ± 0.2001	0.033	0.799	0
PTF09dxw	8.627 ± 0.072	-0.9420 ± 0.2001	-0.598	0.742	0
PTF09dza	8.688 ± 0.072	0.1926 ± 0.2001	-0.197	0.514	0
PTF09edr	8.760 ± 0.083	-0.5293 ± 0.2002	-0.111	1.045	1
PTF09eoi	8.518 ± 0.096	-0.8333 ± 0.2008	-0.454	0.211	0
PTF09fox	8.664 ± 0.071	0.5646 ± 0.2000	-0.216	0.243	0
PTF09foz	–	<-1.7998	-0.033	0.735	0
PTF09gce	8.835 ± 0.073	-0.2271 ± 0.2001	-0.189	0.745	0
PTF09gon	–	<-1.4682	0.052	0.994	0
PTF09gul	8.804 ± 0.074	-0.4125 ± 0.2001	-0.212	0.831	1
PTF09hpl	8.710 ± 0.072	0.5366 ± 0.2001	-0.292	0.674	0
PTF09hpq	–	<-2.1847	0.122	0.932	0
PTF09hql	8.573 ± 0.081	-1.1066 ± 0.2001	-1.132	0.564	0
PTF09hqp	8.826 ± 0.070	0.8022 ± 0.2000	-0.132	0.585	0
PTF09ifh	8.724 ± 0.093	0.1958 ± 0.2008	-0.513	0.837	0
PTF10aaiw	8.854 ± 0.070	-0.6567 ± 0.2001	-0.349	0.944	0
PTF10accd	8.362 ± 0.087	-0.8841 ± 0.2002	-1.046	0.374	0
PTF10acnz	8.799 ± 0.079	-0.7896 ± 0.2023	0.074	0.890	1
PTF10bxs	8.718 ± 0.075	0.4785 ± 0.2002	-0.530	0.771	0
PTF10duz	8.571 ± 0.074	0.3213 ± 0.2001	-0.511	0.398	0
PTF10fps	8.751 ± 0.071	0.4652 ± 0.2000	0.083	0.413	0
PTF10fxl	8.752 ± 0.070	0.4853 ± 0.2000	-0.162	0.578	0
PTF10gmd	8.748 ± 0.084	<-1.9430	-0.075	0.722	1
PTF10gmg	8.396 ± 0.078	-0.3354 ± 0.2001	-1.148	0.994	0
PTF10hdn	8.224 ± 0.090	-0.2529 ± 0.2002	-1.297	0.695	0
PTF10hdv	8.101 ± 0.079	-1.1635 ± 0.2005	-1.099	0.734	0
PTF10hjw	8.618 ± 0.073	-0.0162 ± 0.2001	-1.081	0.654	0
PTF10hml	8.506 ± 0.077	0.0052 ± 0.2001	-0.210	0.249	0
PTF10icb	8.438 ± 0.074	-0.1586 ± 0.2001	-0.474	0.348	0

Table 5 – *continued*

SN name	12+log(O/H)	logSFR ($M_\odot$ yr^{-1})	[M/H]	logAge (Gyr)	AGN[b]
		Host spectroscopic properties[a]			
PTF10iyc	8.740 ± 0.087	-0.4100 ± 0.2002	-0.306	1.052	0
PTF10jdw	8.738 ± 0.089	0.4382 ± 0.2006	-0.605	0.765	0
PTF10jtp	8.779 ± 0.078	0.9699 ± 0.2001	-0.201	0.827	0
PTF10mwb	–	-1.3801 ± 0.2001	-1.179	0.605	0
PTF10nkd	8.570 ± 0.082	-0.6267 ± 0.2003	-1.116	0.614	0
PTF10nlg	8.552 ± 0.071	-0.2332 ± 0.2000	0.013	-0.252	0
PTF10pvi	8.621 ± 0.167	0.1395 ± 0.2034	-0.835	0.826	0
PTF10qjl	8.191 ± 0.214	0.0953 ± 0.2022	-0.905	0.730	0
PTF10qjq	8.678 ± 0.070	0.5050 ± 0.2000	-1.005	0.621	0
PTF10qkf	8.680 ± 0.087	-0.0993 ± 0.2003	-0.876	0.723	0
PTF10qkv	8.755 ± 0.082	0.0145 ± 0.2003	-0.209	0.810	0
PTF10qky	8.675 ± 0.071	0.7003 ± 0.2000	-0.073	0.312	0
PTF10qny	8.645 ± 0.078	0.7040 ± 0.2002	-0.408	0.404	0
PTF10qsc	–	-0.3717 ± 0.2006	-0.320	0.755	0
PTF10qwg	8.727 ± 0.072	-0.0504 ± 0.2000	-0.363	0.905	0
PTF10rab	8.098 ± 0.067	-1.3371 ± 0.2000	–	–	0
PTF10rbp	8.816 ± 0.075	0.2401 ± 0.2001	-0.153	0.665	0
PTF10tce	8.663 ± 0.145	-0.1912 ± 0.2030	-0.185	0.707	0
PTF10trp	8.623 ± 0.072	-0.0145 ± 0.2001	-0.860	0.534	0
PTF10twd	8.505 ± 0.072	0.0067 ± 0.2000	-0.693	0.572	0
PTF10ubm	8.664 ± 0.070	0.2402 ± 0.2000	-0.573	0.626	0
PTF10viq	8.822 ± 0.076	1.0179 ± 0.2003	-0.025	0.558	0
PTF10wnm	8.697 ± 0.119	0.4628 ± 0.2018	-0.131	0.482	0
PTF10wnq	–	<-1.0496	-0.130	1.035	0
PTF10wof	8.575 ± 0.100	-0.1685 ± 0.2011	-1.035	0.803	0
PTF10wor	8.903 ± 0.057	-0.7775 ± 0.2008	0.071	0.939	1
PTF10wos	–	<-2.0219	-0.117	0.916	0
PTF10xyt	8.397 ± 0.078	-0.4585 ± 0.2001	-1.047	0.443	0
PTF10yer	8.624 ± 0.071	0.4392 ± 0.2000	-1.011	0.781	0
PTF10ygu	–	0.4154 ± 0.2041	-0.420	0.834	0
PTF10yux	8.711 ± 0.085	-0.6406 ± 0.2002	-0.199	0.922	1
PTF10zbk	8.768 ± 0.071	-0.0288 ± 0.2000	-0.203	0.820	0
PTF10zdk	8.431 ± 0.101	-0.4892 ± 0.2001	-0.402	0.005	0
PTF10zgy	8.827 ± 0.072	0.9997 ± 0.2000	0.010	0.601	1
PTF11apk	8.829 ± 0.074	-0.7912 ± 0.2002	-0.005	0.981	1
PTF11atu	8.559 ± 0.086	-0.6486 ± 0.2005	-0.842	0.711	0
PTF11bas	–	0.0040 ± 0.2270	-1.084	0.735	0
PTF11bju	8.363 ± 0.072	-0.4429 ± 0.2000	-0.893	0.304	0
PTF11htb	8.235 ± 0.181	-0.6434 ± 0.2006	-1.135	0.640	0
PTF11khk	8.777 ± 0.081	0.4498 ± 0.2012	0.095	0.599	0
PTF11kjn	8.816 ± 0.074	-0.3221 ± 0.2010	0.108	0.993	1
PTF11kx	8.679 ± 0.072	-0.1617 ± 0.2001	-0.737	0.303	0
PTF11lih	8.747 ± 0.150	1.4264 ± 0.2038	-0.212	0.907	0
PTF11mty	8.584 ± 0.082	0.7431 ± 0.2004	-0.100	0.346	0
PTF11okh	8.811 ± 0.074	-0.0839 ± 0.2001	0.117	1.056	0
PTF11opu	8.319 ± 0.175	0.1381 ± 0.2024	-0.857	0.721	0
PTF11pfm	8.406 ± 0.070	-1.1024 ± 0.2000	-0.193	0.261	0
PTF11v	8.795 ± 0.076	-0.7488 ± 0.2004	-0.014	1.078	1
PTF11vl	8.581 ± 0.093	-0.6123 ± 0.2004	-1.020	0.664	0

[a]The host parameters determined either from emission line or stellar continuum measurements.
[b]The AGN tags for the host galaxies in this work. Normal galaxies are labelled as 0 and AGN hosts are labelled as 1.

3.3.2 Gas-phase metallicity

There are various methods for calibrating the gas-phase metallicity determined by emission line ratios (for a review see Kewley & Ellison 2008, hereafter KE08). The direct method is to measure the ratio of the [O III] λ4363 line to a lower excitation line to estimate the electron temperature (T_e) of the gas, and then convert it to the metallicity – the so-called T_e-based metallicity. The disadvantage is that this [O III] line is very weak and difficult to detect unless a very high S/N spectrum can be acquired; in our sample for only three spectra was the [O III] λ4363 line detected. Instead, we use indirect metallicity calibrations, and, following the recommendation of KE08, adopt the empirical relations from Pettini & Pagel (2004, hereafter PP04). PP04 fit the relations between various emission line ratios and the T_e-based metallicity measurement for a sample of H II regions.
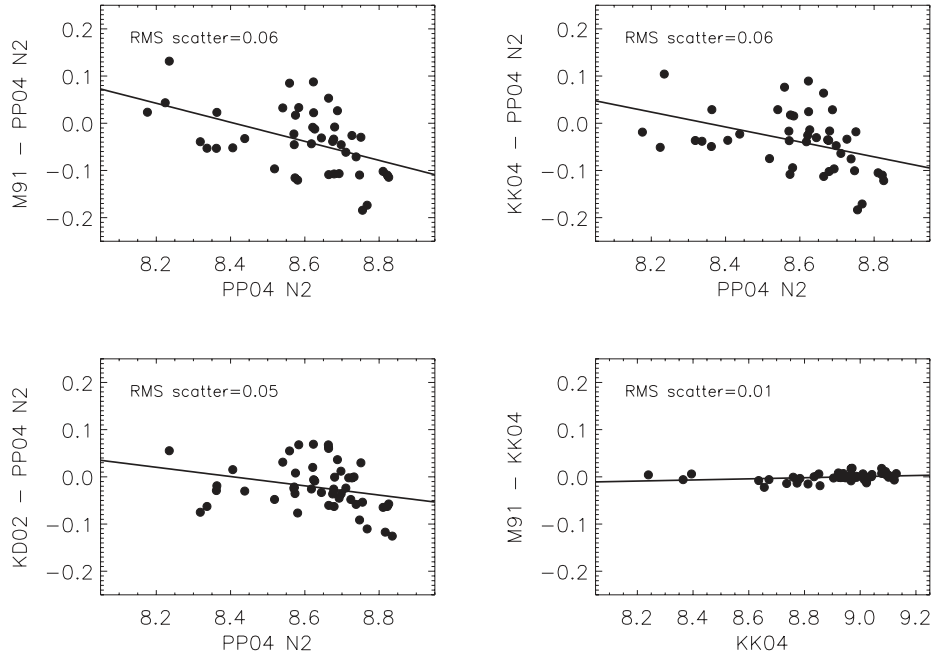
Figure 5. The metallicity conversions used in this paper. We convert the metallicities derived by M91, KK04 and KD02 to PP04 N2, which is the calibration used for our host galaxy data. In each plot, we use the best linear fit (solid line) and scatter to represent the accuracy of the conversion.

The PP04 'N2' method uses the ratio of [N II] $\lambda6584$ to Hα. As these lines are very close in wavelength space, this is a (nearly) reddening-free method, and covers both the upper branch $(\log([\text{N II}]/[\text{O II}]) > -1.2)$ and lower branch $(\log([\text{N II}]/[\text{O II}]) < -1.2))$ metallicities. The PP04 relation is only valid for $-2.5 < \text{N2} < -0.3$. Gas-phase metallicities for 53 galaxies in our sample can be derived using this method.

For those galaxies outside the valid range of PP04 'N2' method, we follow the Kewley & Dopita (2002, hereafter KD02) method. Unlike the empirical PP04 calibration, the KD02 technique is derived based on stellar evolution and photoionization models. For the upper branch metallicities, we use the ratio of [N II] and [O II] $\lambda3727$, and for the lower branch metallicity, KD02 recommend averaging two methods based on the R_{23} ratio $(([\text{O II}] + \text{O III} \lambda4959, 5007)/\text{H}\beta)$: the McGaugh (1991, hereafter M91) and Kobulnicky & Kewley (2004, hereafter KK04) relations. For the 29 galaxies where metallicities are unavailable via the PP04 N2 method, 19 can be calibrated following KD02. The 10 other galaxies show no detectable emission lines available for the metallicity calibration.

As previous studies have noted, offsets may exist between these different metallicity calibrations and thus we used the self-consistent calibrations of KE08. For galaxies where it is possible to make more than one metallicity measurement, we can also compare the results directly. This is shown in Fig. 5; the different calibrations after applying a linear fit compare well. The observed rms scatters are (this work/KE08): 0.06/0.07, 0.06/0.07, 0.05/0.05 and 0.01/0.02 for the M91–PP04, KK04–PP04, KD02–PP04 and M91–KK04 relations, respectively. The best-fitting linear trends (the difference between two different metallicity calibrations) are applied to our metallicity measurements, although they have no significant effects on the final results.

3.3.3 Stellar metallicity and age

The stellar metallicity and age are normally determined using absorption features in the spectrum. One widely used method is the

Lick/IDS system (Worthey 1994; Trager et al. 1998). Recently, with the availability of high-quality model templates, the 'full spectrum fitting' method has become a popular alternative (e.g. Cid Fernandes et al. 2005; Koleva et al. 2009) to study the stellar populations, as it exploits more spectral information than just individual line indices.

In this study, we use PPXF to fit the stellar continuum of our host spectra. The same MILES templates described in Section 3.1 were used. One feature of PPXF is the linear regularization performed during the fit, which can help smooth the weights of the best-fitting templates. However, this feature must be used with caution, as it is a trade-off between the smoothness and goodness of the fit. Following the procedure described in Press et al. (1992), the regularization parameter for each host galaxy was determined such that the resulting fit was consistent with the observations, but also gave a smooth star formation history. Finally, the stellar metallicity and age can be estimated by performing a weighted-average of all the model templates, given by

$$\langle \log t \rangle = \sum_{i=1}^{N} w_i \times \log t_i \tag{5}$$

and

$$\langle [\text{M/H}] \rangle = \sum_{i=1}^{N} w_i \times [\text{M/H}]_i, \tag{6}$$

where $\log t_i$, $[\text{M/H}]_i$ and w_i represent the stellar age, stellar metallicity and weight of the ith template. The $\langle \log t \rangle$ and $\langle [\text{M/H}] \rangle$ are the mass-weighted age and metallicity over the N templates used to fit the spectrum. Here, we estimated the uncertainty by examining the dispersion between the results with and without regularization. An uncertainty of 0.12 dex and 0.15 dex was determined and added to [M/H] and stellar age, respectively.

A comparison between the host gas-phase and stellar metallicities can be found in Fig. 6. It is clear that the two metallicities scale with each other with a positive Pearson correlation coefficient $\sim$0.67.
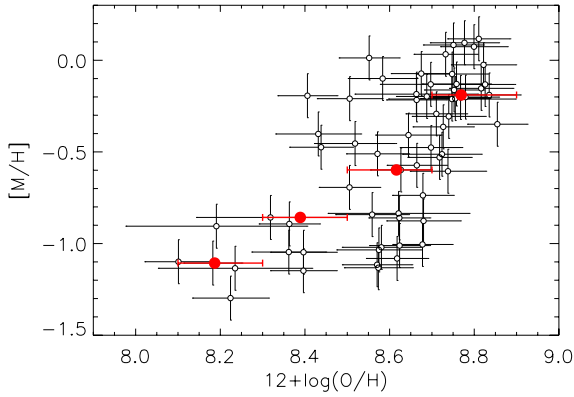
Figure 6. The host stellar metallicity as function of gas-phase metallicity. The median metallicity in each bin with bin size = 0.2 dex is computed and shown in red filled-circle.

3.3.4 Host stellar mass

The final parameter of interest is the stellar mass of the host galaxies. We use the photometric redshift code Z-PEG (Le Borgne & Rocca-Volmerange 2002), which is based on the spectral synthesis code PÉGASE.2 (Fioc & Rocca-Volmerange 1997), to estimate $M_{stellar}$. Z-PEG fits the observed galaxy colours (Section 2.5) with galaxy SED templates corresponding to nine spectral types (SB, Im, Sd, Sc, Sbc, Sb, Sa, S0 and E). We assume a Salpeter (1955) IMF. A foreground dust screen varying from a colour excess of $E(B - V) = 0$ to 0.2 mag in steps of 0.02 mag is used.

Z-PEG is used to locate the best-fitting SED model (in a χ^2 sense), with the redshift fixed at the redshift of the SN host galaxy measured from our spectra. The current $M_{stellar}$ and the recent SFR, averaged over the last 0.5 Gyr before the best-fitting time step, are recorded. Error bars on these parameters are taken from their range in the set of solutions that have a similar χ^2 (as in Sullivan et al. 2006). Note that these SFRs are not used in the analysis in this paper.

The main uncertainty in this procedure is the choice of SED libraries used in the χ^2 fitting. We use the standard Z-PEG libraries for ease of comparison to previous results in the literature. However,

we note that improved stellar masses can be obtained by the use of more recent templates (Johansson et al. 2013), particularly those that include an improved treatment of the thermally pulsing asymptotic giant branch stage of stellar evolution (Maraston 2005). A fuller discussion of the uncertainties associated with this stellar population modelling can be found in Childress et al. (2013b). These authors conservatively concluded that the maximal systematic is ∼0.4 dex in $M_{stellar}$, which should be borne in mind when interpreting our results.

Fig. 7 shows a comparison between the SFRs derived from the Hα line to that estimated by Z-PEG. The mean difference in log(SFR) is ∼0.25 dex, with the SFRs from Z-PEG systematically larger than those from the Hα luminosity. A similar offset using similar techniques was also found by Smith et al. (2012). This offset is perhaps not surprising; Z-PEG determines SFRs essentially from u-band data and is therefore sensitive to SFRs over a longer time-period than the instantaneous Hα-based measures.

The relation between the spectroscopic SFRs and $M_{stellar}$ for our sample is shown in Fig. 7. We overplot the relation determined by the Galaxy And Mass Assembly survey (Foster et al. 2012), which used a similar method as ours for estimating the SFR. Our results show good consistency with this relation, although we also sample some massive galaxies with lower SFRs than the linear relation would predict.

Finally, in Fig. 8 we plot our metallicities as a function of $M_{stellar}$ (the 'mass–metallicity relation'). The mass–metallicity relation studied by KE08 using the PP04 N2 method is overplotted for comparison. For consistency, in this plot we have adopted the same IMF (Kroupa 2001) and cosmology ($H_0 = 72$ km s^{-1} Mpc^{-1} and $\Omega_M = 0.29$) as used by KE08 for the measurement of $M_{stellar}$. It is clear that our SN Ia host galaxies follow a very similar mass–metallicity relation as that of KE08. This will be considered further in Section 5.2.

4 THE DEPENDENCE OF SN Ia PROPERTIES ON THEIR HOST GALAXIES

Having measured various physical parameters of the PTF SN Ia host galaxies from their spectra and broad-band photometry, we
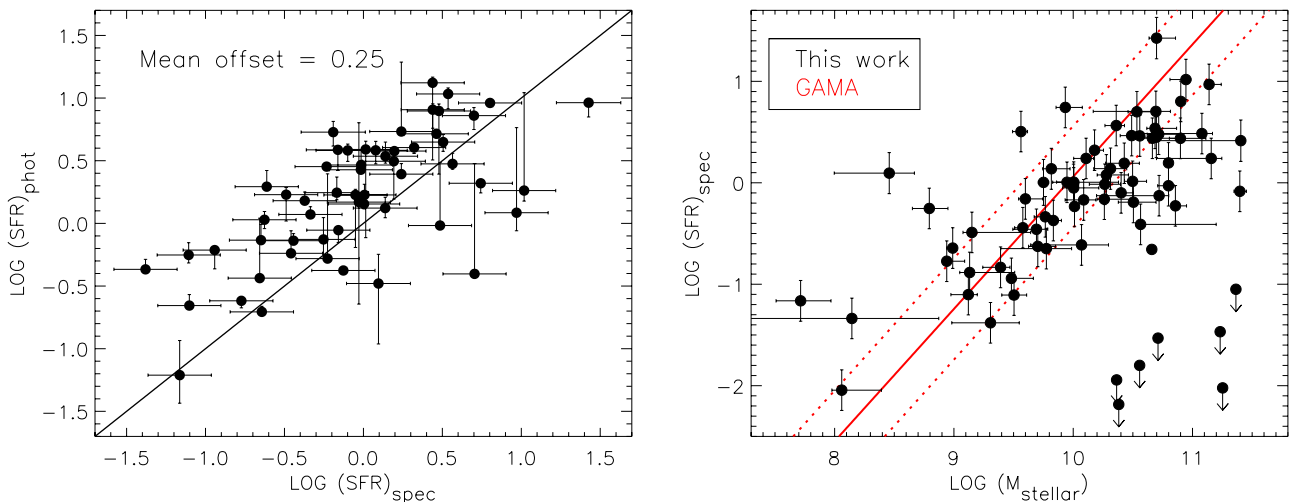
Figure 7. Left: a comparison of the star formation rates (SFRs) derived from Hα luminosities (SFR$_{spec}$) to those measured from broad-band photometry using Z-PEG (SFR$_{phot}$). The solid line shows the 1:1 relation. Right: the SFR measured from Hα as function of the host $M_{stellar}$. The relation determined by the Galaxy And Mass Assembly survey (GAMA; Foster et al. 2012) is overplotted. The dotted line shows the 1σ range of the GAMA relation. Some passive galaxies with a low SFR for their $M_{stellar}$ (i.e. a low specific SFR) can be seen for large $M_{stellar}$.
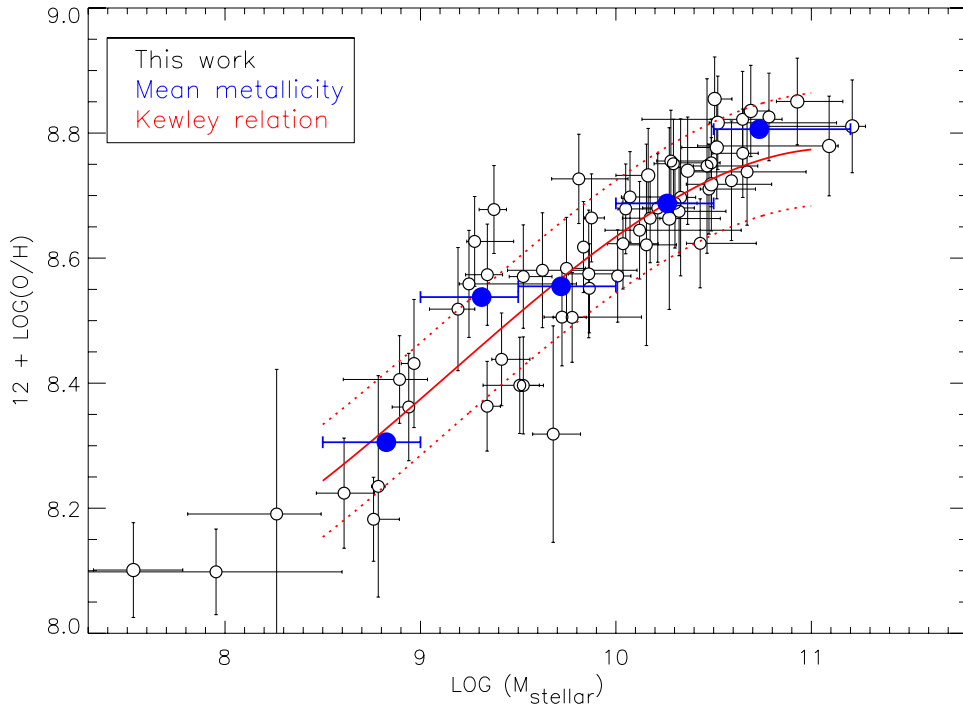
Figure 8. The $M_{stellar}$–metallicity relation derived for our host galaxy sample. The red solid line is the best fit from KE08 using the PP04 N2 metallicity calibration. The red dotted lines represent the rms residuals from the best fit to field galaxies. The mean metallicity (blue filled circle) in each bin is also computed.

now compare these parameters with the photometric properties of the SNe. We take each of the three key SN Ia properties in turn – stretch (light-curve width), optical colour and luminosity – and compare with the $M_{stellar}$, the gas-phase metallicity $12 + \log(O/H)$, the stellar metallicity M/H, the stellar age and the specific SFR (sSFR), the SFR per unit $M_{stellar}$ (Guzman et al. 1997). Compared to the SFR, the sSFR is a more appropriate indicator to measure the relative star formation activity of a galaxy as it measures the star formation relative to the underlying galaxy stellar mass.

In this section, we will assess the significance of various relations between the SN properties and their host galaxies. In each case, we split the sample into two groups. A value of $\log M = 10.0$ is used to split between the high- and low-$M_{stellar}$ sample, and $12 + \log(O/H) = 8.65$ and $[M/H] = -0.5$ are used (based on the mass–metallicity relation in Fig. 8 and relation between gas-phase and stellar metallicities in Fig. 6) to split between high- and low-metallicity hosts. For the stellar age, SFR and sSFR, the split points were selected to make approximately equally sized sub-groups (e.g. Sullivan et al. 2010). The weighted-mean of the residuals in each group are calculated. The error of the weighted mean was corrected to ensure a $\chi^2_{red} = 1$. The linear fitting is performed by using the Monte Carlo Markov Chain (MCMC) method LINMIX (Kelly 2007). To examine the correlation of the relations, both the Pearson and Kendall correlation coefficients are also calculated.

4.1 SN Ia stretch

The stretch of an SN Ia is a direct measurement of its light-curve width, a key parameter in the calibration of SNe Ia as distance estimators (Phillips 1993) – brighter SNe Ia have slower light curves (a broader width or higher stretch) than their fainter counterparts. In this study, we restrict our analysis to SNe Ia with $0.7 < s < 1.3$, typical of SNe Ia that are used in cosmological analyses (Conley

et al. 2011). This removes one high-stretch and five low-stretch (subluminous) SNe, including the peculiar event PTF09dav (Sullivan et al. 2011a).

The SN stretch as a function of the host parameters can be found in Fig. 9. The trend calculated for each case is listed in Table 6. When comparing with $M_{stellar}$, we recover the trend seen by earlier studies that lower stretch ($s < 1$) SNe Ia are more likely to be found in massive galaxies than higher stretch ($s \geq 1$) SNe Ia (Howell et al. 2009; Neill et al. 2009; Sullivan et al. 2010). Bearing in mind that gas-phase and stellar metallicity strongly correlates with $M_{stellar}$ (e.g. Tremonti et al. 2004; Gallazzi et al. 2005), a similar trend is expected between stretch and metallicity, which is both observed here (Fig. 9) and has previously been described in the literature: low-metallicity galaxies preferentially host brighter SNe Ia (before light-curve shape correction). The data also show that higher stretch SNe Ia preferentially explode in younger galaxies, to the extent that there are few low-stretch SNe in hosts with mass-weighted mean ages of less than ∼4 Gyr. This is consistent with the recent study of Rigault et al. (2013), who found that the relation between SN stretch and $M_{stellar}$ is primarily driven by age, as measured by local SFR. We also see moderate trend with sSFR that galaxies with higher sSFR tend to host brighter SNe Ia. No significant correlation is found with SFR.

4.2 SN Ia colour

We next examine trends with SN Ia colour ($\mathcal{C}$; Section 2.4), shown in Fig. 10. As for the stretch comparisons, we restrict the SNe to a typical colour range used in cosmological studies ($\mathcal{C} < 0.4$). This removes five red SNe Ia from our sample.

As star-forming galaxies are expected to contain more dust than passive galaxies, all other things being equal we would expect them to host redder SNe Ia. However, Fig. 10 does not show this effect;
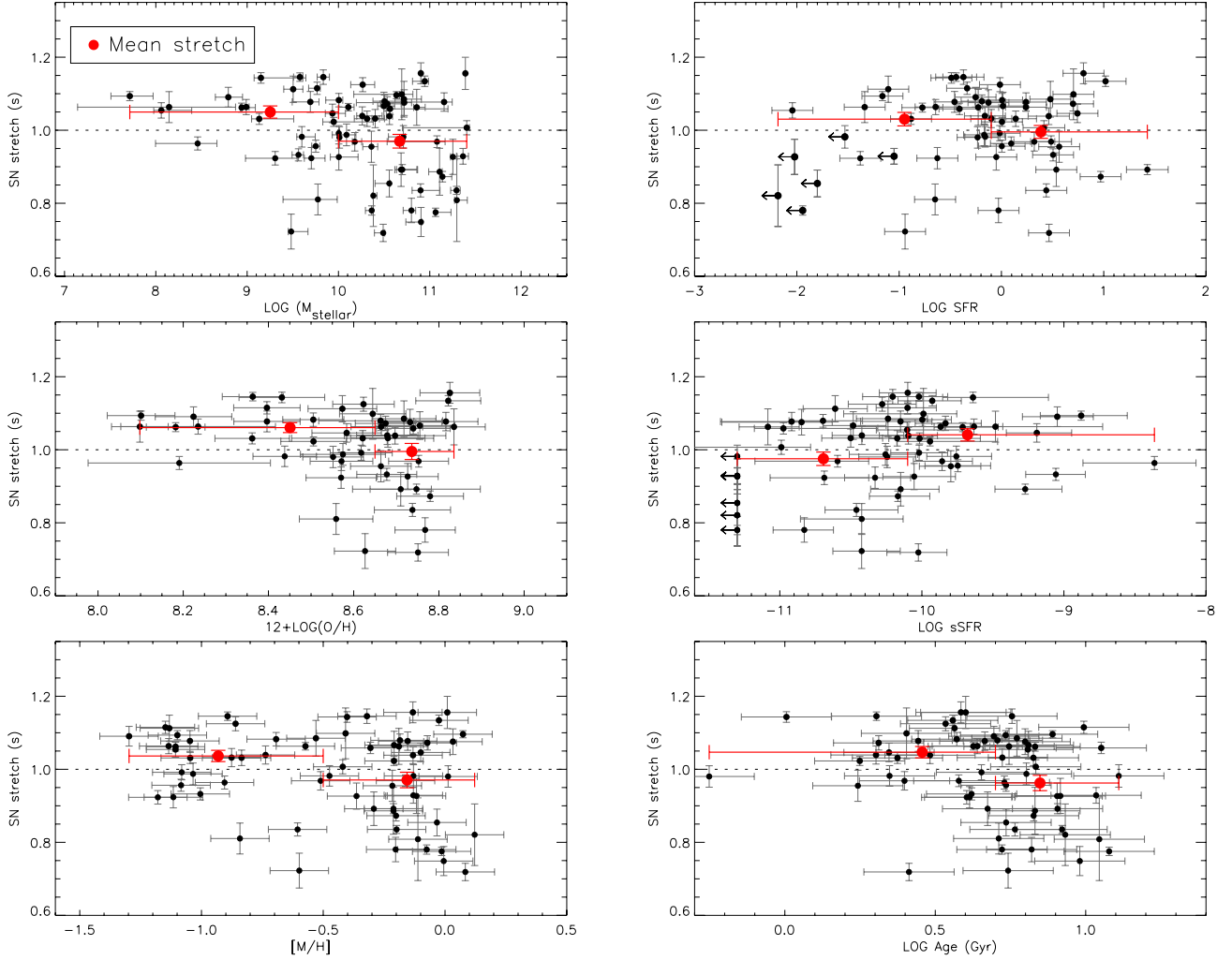
Figure 9. The SN stretch *s* as a function of host M_{stellar} (top left), SFR (top right), gas-phase metallicity (middle left), specific SFR (sSFR; middle right), mass-weighted mean stellar metallicity (lower left) and stellar age (lower right). The red points represent the mean stretch in bins of host parameters.

Table 6. The trend of SN stretch/colour with host parameters.

	Split point	SN stretch (*s*)		SN colour ($\mathcal{C}$)	
		N_{SN}	Bin difference	N_{SN}	Bin difference
log M	10.0	68	0.08 (4.3σ)	55	0.05 (2.5σ)
12+log (O/H)	8.65	50	0.07 (2.5σ)	40	0.05 (2.5σ)
[M/H]	−0.5	67	0.07 (2.5σ)	55	0.06 (3.1σ)
log Age	0.7	67	0.08 (3.2σ)	55	0.01 (0.7σ)
log SFR	−0.1	65	0.03 (1.4σ)	52	0.03 (1.3σ)
log sSFR	−10.1	65	0.08 (3.1σ)	52	0.03 (1.2σ)

if anything SNe Ia in high-sSFR galaxies appear bluer ($\mathcal{C} < 0$) than those in low-sSFR galaxies. This may imply an intrinsic variation of SN colour with host environment that is greater than any reddening effect from dust. The SN colour as a function of M_{stellar} does show a trend, with SNe Ia in more massive galaxies being redder, and both gas-phase and stellar metallicities also show correlations with SN colour with SNe Ia tending to be redder in galaxies of higher metallicity. We will discuss these various trends involving SN colour in Section 5.

4.3 SN luminosity

Finally, we turn to the SN luminosity, which we parametrize by calculating the Hubble residual. This is defined as the difference between m_B^{corr}, the observed rest-frame *B*-band SN apparent magnitude (m_B; Section 2.4) corrected for stretch and colour, and m_B^{mod}, the peak SN magnitude expected in our assumed cosmological model. At a fixed redshift, a brighter SN Ia therefore gives a negative Hubble residual. m_B^{corr} is given by

$$m_B^{\mathrm{corr}} = m_B + \alpha \times (s - 1) - \beta \times \mathcal{C} \qquad (7)$$

and m_B^{mod} by

$$m_B^{\mathrm{mod}} = 5 \log_{10} \mathcal{D}_L (z; \Omega_{\mathrm{M}}) + \mathcal{M}_B, \qquad (8)$$

where *z* refers to the cosmological redshift in the cosmic microwave background (CMB) frame, $\mathcal{D}_L$ is the c/H_0 reduced luminosity distance with the c/H_0 factor (here *c* is the speed of light) absorbed into $\mathcal{M}_B$, the absolute luminosity of a $s = 1$ $\mathcal{C} = 0$ SN Ia (equation 7). Explicitly, $\mathcal{M}_B = M_B + 5 \log_{10}(c/H_0) + 25$, where M_B is the absolute magnitude of a SN Ia in the *B* band. α and β are 'nuisance variables' derived from the cosmological fits. In this work, $\alpha = 1.45 \pm 0.12$ and $\beta = 3.21 \pm 0.15$ were obtained. We do not add
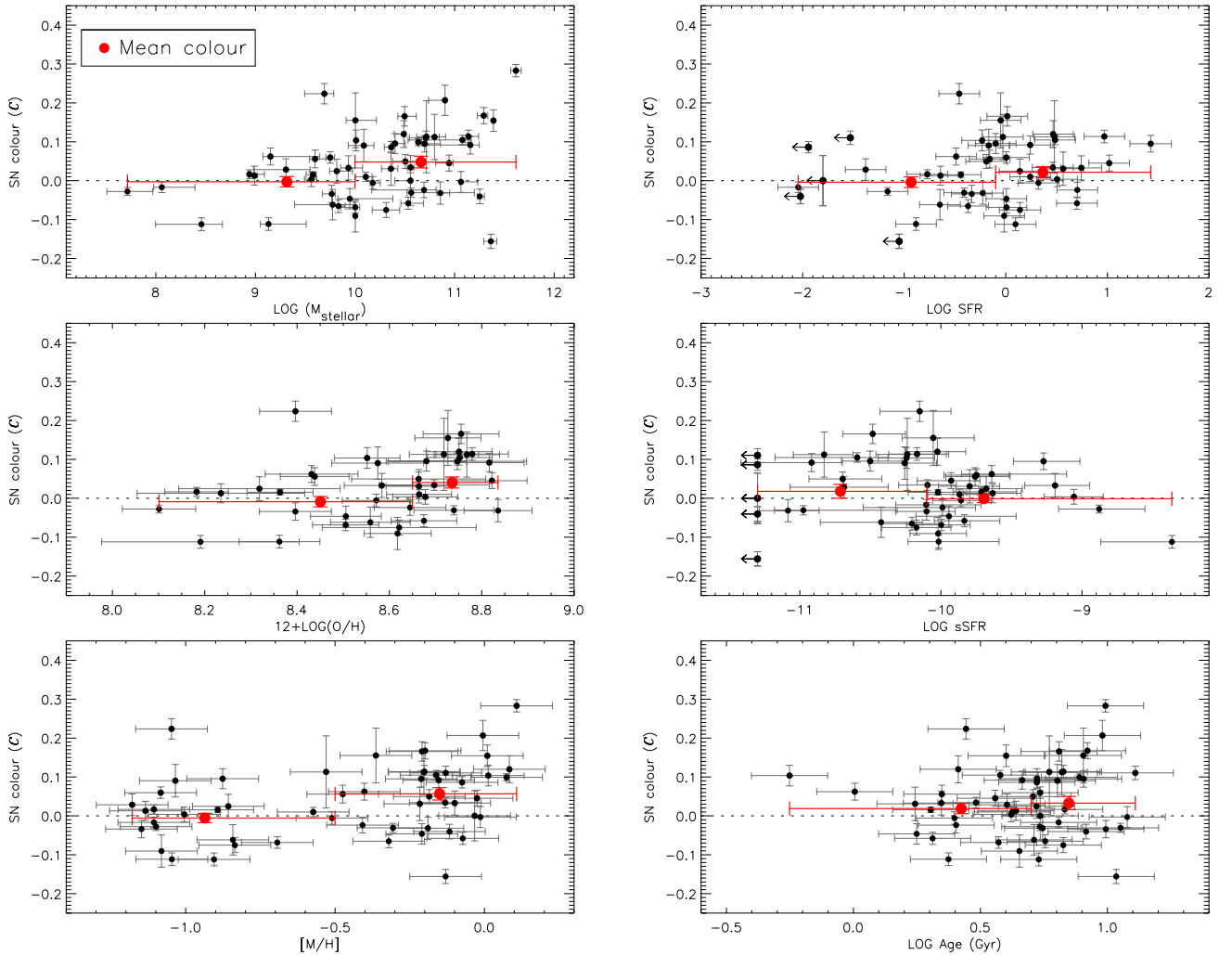
Figure 10. As Fig. 9, but considering the SN colour $\mathcal{C}$ in place of stretch.

any intrinsic dispersion into the Hubble residual uncertainties as we are, in part, searching for variables which could generate this extra scatter. However, we are aware of the potential bias that this could introduce into the nuisance parameters (e.g. α and β) when comparing the results to the studies including the intrinsic dispersion, and thus we caution such a comparison is not valid. To ensure our SNe are located in the smooth Hubble flow, we exclude SNe Ia with $z < 0.015$, removing one SN from our sample. The comparisons with the host galaxy parameters can be found in Figs 11 to 14. The trends calculated for Hubble residuals with host parameters are listed in Table 7.

The Hubble residuals as a function of host $M_{stellar}$ are shown in Fig. 11. We see only a weak trend that is consistent with that expected based on earlier work, in the sense that more massive galaxies preferentially host brighter SNe Ia after stretch and colour corrections. However, the trend in our data taken in isolation is not significant: the Hubble residuals of low-$M_{stellar}$ and high-$M_{stellar}$ bins have a weighted average of 0.057 ± 0.038 mag and -0.028 ± 0.028 mag, respectively, a difference of 0.085 ± 0.047 mag. There is an ∼91 per cent probability the slope is negative based on 10 000 MCMC realizations.

Figs 12 and 13 show the Hubble residuals as a function of gas-phase and stellar metallicity, respectively. A trend with gas-

phase metallicity can be seen in the same sense as with stellar mass: higher metallicity galaxies tend to host brighter SNe Ia after stretch and colour corrections. The differences are more significant than with $M_{stellar}$: the Hubble residuals of the high-metallicity and low-metallicity bins have a weighted average of -0.047 ± 0.030 mag and 0.068 ± 0.035 mag, respectively, a difference of 0.115 ± 0.046 mag. Fitting a straight line using the LINMIX method gives an ∼98 per cent probability the slope is negative. The correlation coefficient is ∼2 times larger than the relation between Hubble residuals and $M_{stellar}$. We see no trend with stellar metallicity.

The Hubble residuals as function of host stellar age are shown in Fig. 14; no significant trends are seen. We also see no trend with sSFR.

4.4 Comparison to previous studies

Many of the relations in the previous section have been studied by different authors using independent samples of SNe Ia. Since $M_{stellar}$ is the most straight forward variable to measure, requiring only broad-band imaging, the most common comparison has been between Hubble residual and $M_{stellar}$, which has been examined with a variety of samples over a large redshift range (Kelly et al.
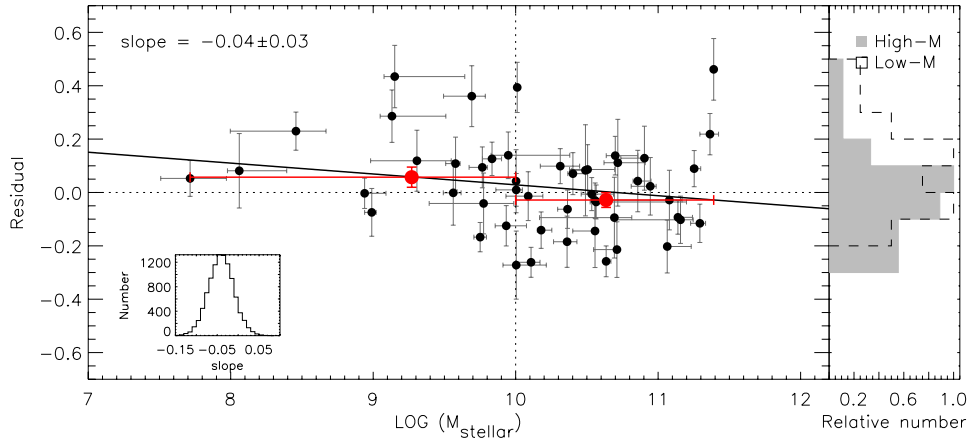
Figure 11. Hubble residuals as a function of host galaxy $M_{stellar}$. The vertical dashed line represents the criterion used to split our sample into high-$M_{stellar}$ and low-$M_{stellar}$ galaxies. The red filled circles represent the weighted mean of the residuals in bins of $M_{stellar}$, and their error bars are the width of the bins and the error of the weighted mean. The histogram on the right shows the distribution of residuals in high-$M_{stellar}$ (filled histogram) and low-$M_{stellar}$ (open histogram). The distribution of the slopes best fitted to the data from 10 000 MCMC realizations was showed in the sub-plot. The solid line represents the mean slope determined from the distribution.
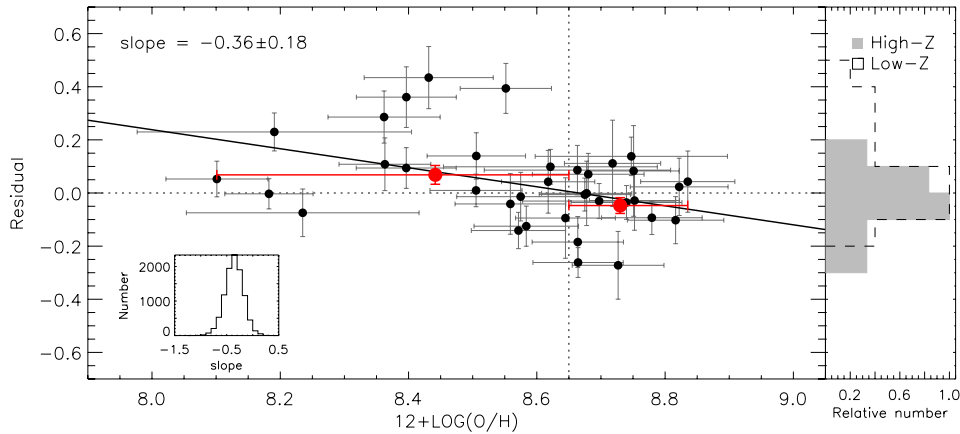
Figure 12. As Fig. 11, but considering gas-phase metallicity instead of $M_{stellar}$.
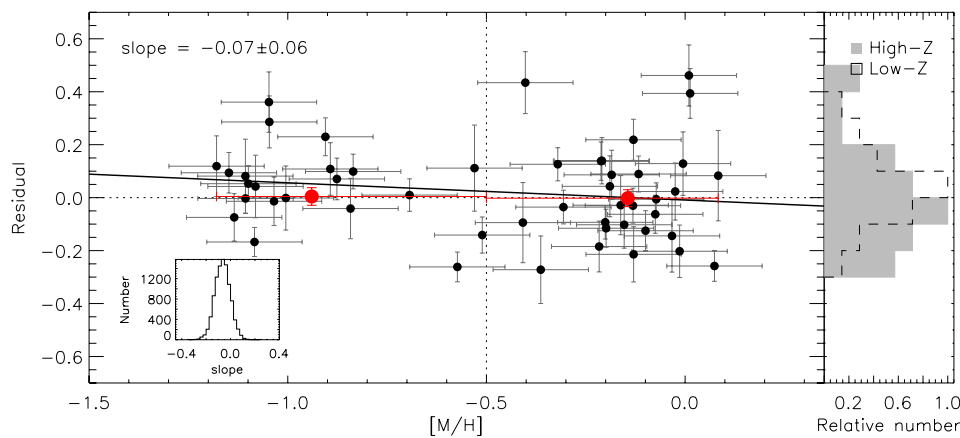
Figure 13. As Fig. 11, but considering stellar metallicity instead of $M_{stellar}$.

2010; Lampeitl et al. 2010; Sullivan et al. 2010; Gupta et al. 2011; Childress et al. 2013b; Johansson et al. 2013). These studies all find that more massive galaxies host brighter SNe after corrections for light-curve shape and colour have been made. The size of the difference is usually around 0.1 mag, with a transition mass of around $10^{10}\,M_{\odot}$. Our result is consistent with these earlier studies, although at a reduced significance due to a smaller data set.

However, our primary goal is to study the metallicity of the SN host galaxies rather than just $M_{stellar}$. Although some studies convert $M_{stellar}$ into metallicity using average mass–metallicity relations
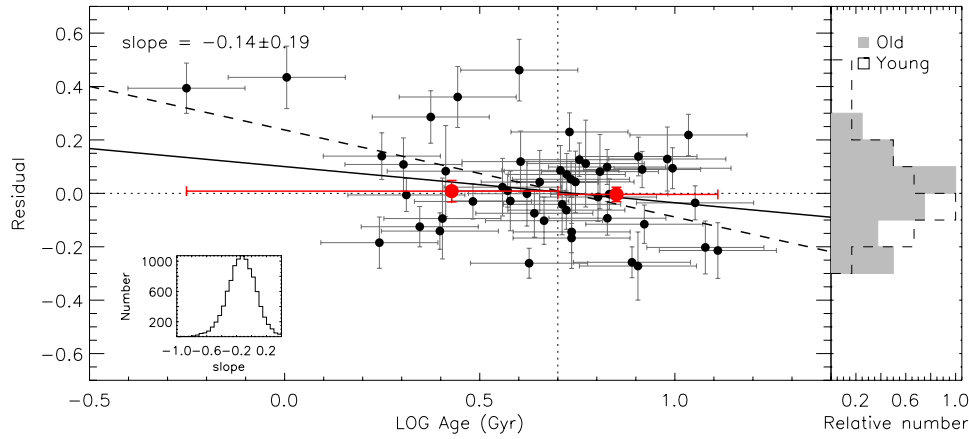
Figure 14. As Fig. 11, but considering stellar age instead of $M_{stellar}$. Here the dashed line includes the two SNe in the youngest host galaxies, which cause a significant trend with Hubble residual, and which otherwise is not present.

Table 7. The trend of Hubble residual with host parameters.

	Split point	N_{SN}	Bin difference (mag)	Linear trend	Probability of negative slope	Correlation Pearson	Kendall
log M	10.0	50	0.085 (1.8σ)	-0.041 ± 0.030	91.3 per cent	-0.19	-0.13
12+log (O/H)	8.65	36	0.115 (2.5σ)	-0.358 ± 0.176	98.1 per cent	-0.36	-0.22
[M/H]	-0.5	50	0.006 (0.1σ)	-0.065 ± 0.063	85.1 per cent	-0.13	-0.09
log Age	0.7	48	0.012 (0.3σ)	-0.135 ± 0.193	75.7 per cent	-0.14	-0.04
log sSFR	-10.1	48	0.070 (1.7σ)	-0.019 ± 0.077	58.7 per cent	0.04	-0.05

(e.g. Sullivan et al. 2010), it is obviously more useful to measure the metallicity directly. The first study of this kind was Gallagher et al. (2005) who compared the Hubble residuals for 16 local SNe Ia with the gas-phase metallicity of their hosts; no significant trends were seen. D'Andrea et al. (2011) studied a larger sample of ~40 SNe Ia host galaxies from the SDSS-II SN survey, finding SNe Ia in high-metallicity galaxies to be ~0.1 mag (≃4.9σ) brighter than those in low-metallicity galaxies after corrections, consistent with the results based on $M_{stellar}$. Using the low-redshift SNe studied by the SNfactory, Childress et al. (2013b) derived the gas-phase metallicity from 69 SNe Ia hosts and found a difference ~0.1 mag (≃2.9σ) difference between high-metallicity and low-metallicity hosts. Our results are in good agreement (a 0.115 mag difference between high- and low-metallicity hosts). Compared to a metallicity simply converted from host $M_{stellar}$, the SN Ia luminosity shows a stronger dependence on the metallicity derived via direct emission-line measurements.

For stellar metallicity studies, Gallagher et al. (2008) studied 29 early-type SN Ia host galaxies by measuring the Lick indices from the SN Ia host spectra. They found the host stellar metallicity correlates with the Hubble residual at ≃98 per cent confidence level, although this technique is not directly comparable to ours. Johansson et al. (2013) also derived the host stellar metallicity by measuring the absorption line indices from the SN Ia host spectra, but did not find a significant trend. We also find no significant trend in our data.

Gupta et al. (2011) determined the mass-weighted average age of 206 SNe Ia host galaxies by fitting their broad-band photometry. They found a weak correlation between the Hubble residuals and host age at ~1.9σ. Johansson et al. (2013) measured the light-weighted age for the SNe Ia host galaxies using the absorption line indices but found no significant trend; again we find no trend in our data.

Sullivan et al. (2010) measured photometric-based sSFRs and found that SNe Ia in low-sSFR hosts appear brighter than those in high-sSFR hosts at ≃2.6σ significance after s and $\mathcal{C}$ corrections. Similar trends have also been found using spectroscopy-based sSFRs (D'Andrea et al. 2011; Childress et al. 2013b). We do not see these trends in our data set although this may be due to the relatively small sample size.

Finally, Rigault et al. (2013) have recently shown that at least some of the trends with host $M_{stellar}$ may be driven by SNe in locally passive environments: SNe in massive galaxies with locally passive environments are systematically brighter than those in locally star-forming environments by ~0.09 mag. At the time of writing, it is unclear whether this trend is due to age or metallicity.

5 DISCUSSION

5.1 The host stellar mass distribution

Unlike galaxy-targeted supernova surveys that are biased towards surveying brighter and more massive galaxies, the host galaxies in rolling searches such as PTF should represent a wider range of SN environments. A key test of this is the host galaxy stellar mass distribution (Fig. 1; Section 2), the form of which should be a combination of the underlying galaxy stellar mass function (GSMF) and the mean SN Ia rate as a function of stellar mass, and which should be able to be reproduced from a qualitative knowledge of both. We examine this in this section.

We begin with the GSMF in the local universe, defined as the number of galaxies per logarithmic bin in stellar mass. For this
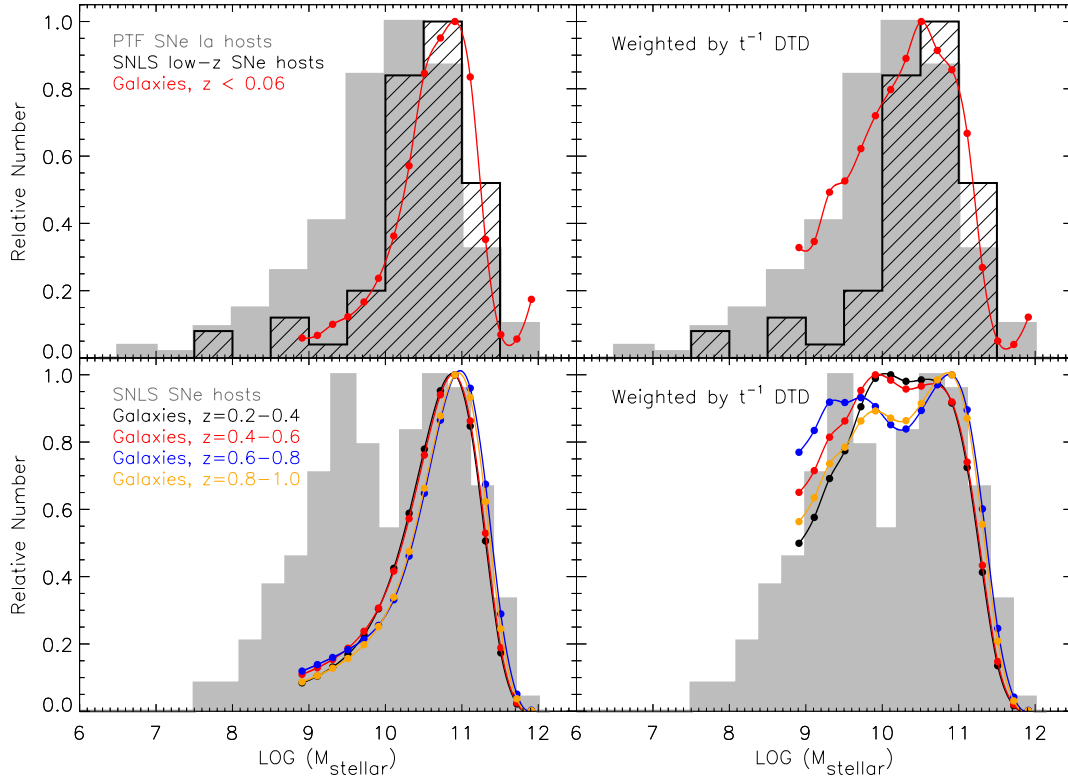
Figure 15. Upper left: the stellar mass distribution of PTF SN Ia host galaxies (grey histogram) compared to the low-redshift SN Ia host sample of Conley et al. (2011; black histogram). The red solid line with filled circles is the predicted distribution based on the stellar mass function of local galaxies ($z < 0.06$; Baldry et al. 2012). Upper right: the same plot as the upper left panel, but with the predicted SN Ia stellar mass distribution produced by weighting each bin by a t^{-1} DTD. Lower left: the stellar mass distribution of the SNe Ia host galaxies in the SNLS sample of Sullivan et al. (2010; grey histogram). The lines with filled circles in different colours represent the mass contributions derived from the galaxy stellar mass functions in different redshift ranges studied by Drory et al. (2009). Lower right: the same plot as left-hand panel, but with prediction weighted by the t^{-1} DTD.

study, we adopt the GSMF of Baldry et al. (2012), the redshift range of which ($z < 0.06$) is similar to this work. In each bin in stellar mass, we divide the GSMF by the total mass (stellar mass multiplied by the GSMF) in that bin. We then overplot the observed SN Ia host galaxy stellar mass distribution. We compare both to an SN Ia host mass distribution drawn primarily from galaxy-targeted searches (the low-z sample compilation of Conley et al. 2011). The result can be seen in the upper left panel of Fig. 15.

The host stellar mass distribution for the galaxy-targeted SN Ia sample is similar to that expected based on the GSMF, but is obviously different to our PTF sample at smaller stellar masses. However, this test assumes that the SN Ia rate is simply proportional to the stellar mass of the host. While this may be approximately correct in the more massive systems, it is known to be incorrect in lower stellar mass systems which have a larger fraction of younger potential progenitor systems or higher sSFRs (Fig. 7) – the SN Ia rate is not simply proportional to stellar mass (e.g. Mannucci et al. 2005; Mannucci, Della Valle & Panagia 2006; Sullivan et al. 2006; Smith et al. 2012). In practice, a delay-time distribution (DTD; the distribution of times between the progenitor star formation and the subsequent SN Ia explosion) with the SN Ia rate proportional to t^{-1} is favoured by most recent data (e.g. Maoz & Mannucci 2012). If we assume this DTD, and the relation between $M_{stellar}$ and galaxy age determined by Gallazzi et al. (2005), a revised distribution of SN Ia host galaxy stellar masses can be formed by weighting each mass bin by a t^{-1} DTD.

The results are shown in Fig. 15 (upper right): the effect of the t^{-1} DTD is to increase the contribution from SNe in less massive (younger) galaxies. A χ^2 is calculated between galaxy stellar mass distribution and SN Ia host galaxy stellar mass distribution. The χ^2 drops from 123.18 to 12.21 (with 5 degrees of freedom) after considering a t^{-1} DTD to the galaxy stellar mass distribution. Indeed, assuming a t^{-1} DTD and a simple scaling between stellar mass and age allows an excellent reproduction of the observed host galaxy stellar mass distribution.

A similar comparison can be made to the stellar mass distribution from the SNLS sample (Sullivan et al. 2010). As seen in the lower panels of Fig. 15, the SNLS sample contains lower stellar-mass galaxies than our PTF sample even though the selection of SNe should be similar. Using the GSMF of Drory et al. (2009) over $0.2 < z < 1.0$, and the same technique as above, again good agreement between the observed host galaxy $M_{stellar}$ distribution and that derived from the GSMF is achieved. Thus, the difference in the stellar mass distributions of the PTF and SNLS host galaxies can be explained by evolution in the field galaxy population from which the hosts are drawn where there is an excess in low-mass galaxies for the stellar mass distributions at high redshifts.

5.2 The mass–metallicity relation of SN Ia host galaxies

As well as impacting on the observed photometric properties of SNe Ia, the metallicity of the progenitor star may also impact on the SN

Ia rate. An increased rate with lower metallicity may be expected as stars with a lower metallicity generally form more massive white dwarfs and therefore may more easily approach the Chandrasekhar mass limit (Kistler et al. 2013). A decreased rate with lower metallicity may be expected in some single degenerate scenarios as the lower metallicity inhibits accretion on to the white dwarf due to lower opacities in the wind (Kobayashi et al. 1998; Kobayashi & Nomoto 2009). Observationally, there is some evidence that prompt SNe Ia are more prevalent (or explode with a brighter luminosity) in metal-poor systems (Cooper, Newman & Yan 2009).

Such effects may impact on the observed SN Ia host mass–metallicity relation; if any of the putative metallicity effects lead to SNe Ia preferentially occurring in low- or high-metallicity galaxies, then the mass–metallicity relation for SN Ia hosts would be offset from that of field galaxies (e.g. at fixed galaxy stellar mass, the SN Ia host galaxies may systematically have lower or higher metallicities than the field galaxies). We compare our mass–metallicity relation with those derived for field galaxies (Fig. 8), and compare the use of four different gas-phase metallicity calibrations in Fig. 16. We fit these mass–metallicity relations using the same functional form as described in KE08 at $8.5 < \log M < 11.0$. Note that although we estimate $M_{stellar}$ by fitting broad-band photometry instead of using the spectroscopic indices of KE08, previous work has shown that the two different approaches provide consistent results (0.001 dex; Smith et al. 2012). Thus, the different $M_{stellar}$ determination techniques should have a negligible effect on our results.

The SN Ia host mass–metallicity relations are consistent with the fits from KE08, with weighted mean offset ∼0.01 dex ($\lesssim 1\sigma$ significance). This is consistent with Childress et al. (2013a), who found that SN Ia hosts in their sample also show good agreement with field galaxy mass–metallicity relation.

However, this comparison has one potential systematic – at fixed $M_{stellar}$, other variables may affect the SN Ia rate, for example the number of young stars (or the SFR). Indeed, Mannucci et al. (2010) showed that the observed mass–metallicity relation could be a projection of a more general relation between $M_{stellar}$, gas-phase metallicity and SFR, which together can be described using a fundamental metallicity relation (FMR). The FMR can be defined as the relation between gas-phase metallicity and $\log(M_{stellar}) - \alpha \times \log(SFR)$, where α is a parameter determined to minimize the scatter of the metallicities. Mannucci et al. (2010) found $\alpha = 0.32$ produced the minimum dispersion in metallicity.

We therefore construct the FMR for the 61 SN Ia hosts with a measure of $M_{stellar}$, SFR and gas-phase metallicity. For comparison, we also determined the FMR for SDSS field galaxies using the same parent sample as Mannucci et al. (2010). Similar quality cuts as described in Mannucci et al. (2010) have been performed. In addition, we applied aperture corrections to the SDSS sample, and select galaxies within a similar redshift range as our host sample (median $z \sim 0.07$). The results are shown in Fig. 17. We found no significant difference between the FMR for SN Ia hosts and that of the SDSS galaxies. The weighted mean
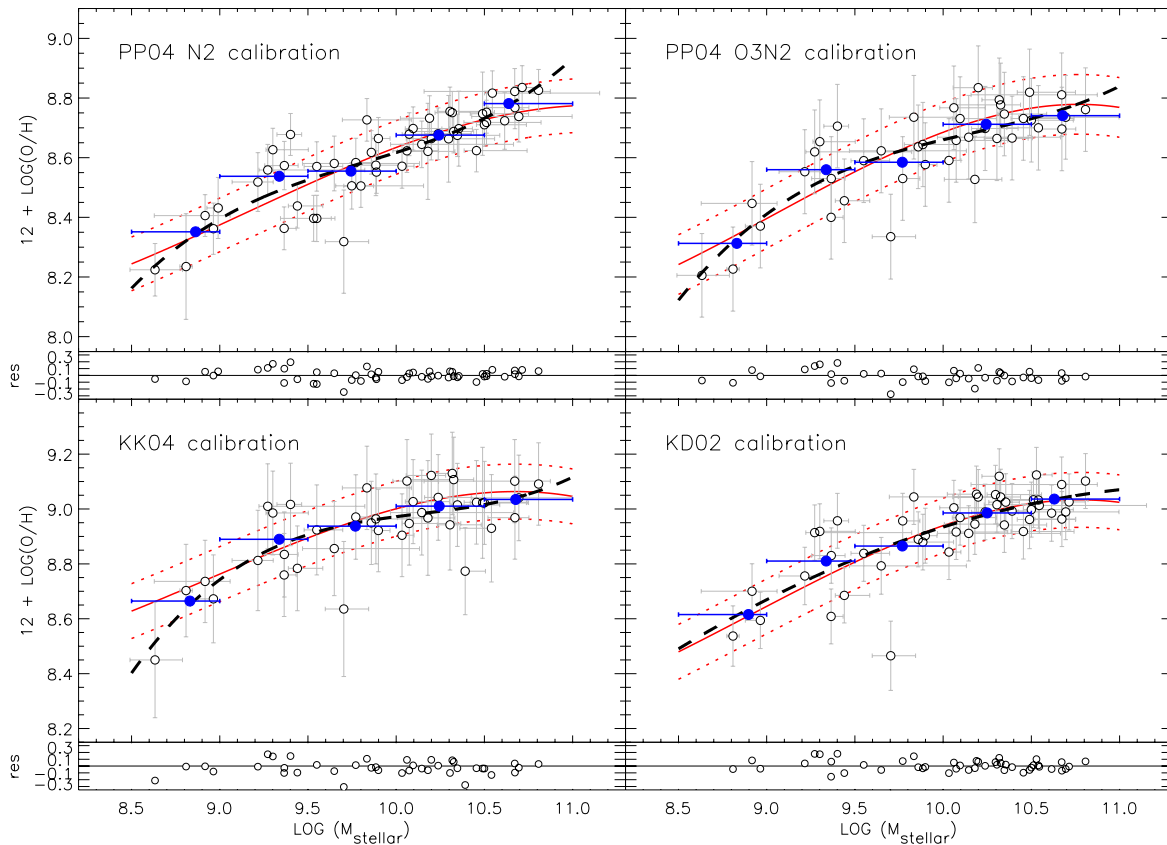

Figure 16. The metallicity–mass relations compared by different metallicity calibrations. Upper panels: PP04 N2 (left) and PP04 O3N2 (right) calibrations. Lower panels: KK04 (left) and KD02 (right) calibrations. The open circles show the measurements in this work. The blue filled circle is the mean metallicity in bins of $M_{stellar}$. The best fit to field galaxies given by Kewley & Ellison (2008) with the range of one rms scatter was overplotted (in red line and red dashed line, respectively). The black dashed line is the best fit to the measurements in this work. The sub-plot in the bottom of each panel represents the residuals of our measurements from KE08's best fit.
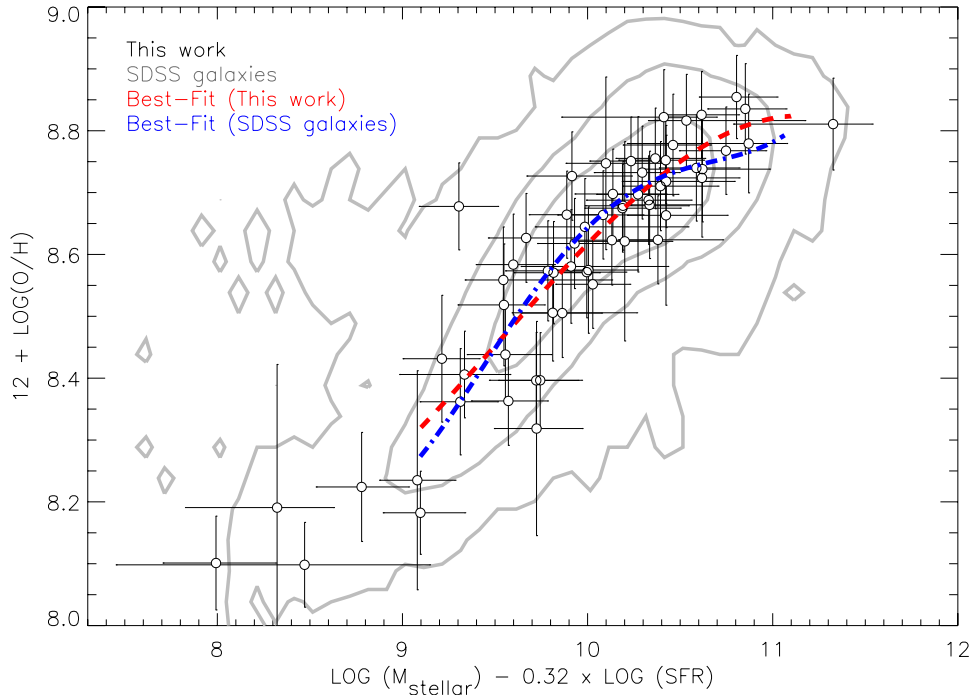
Figure 17. The fundamental metallicity relation (FMR) derived from our data. The open circles show the measurement of SN hosts. The red dashed line is the best fit to it. The grey contours show the sample including 68 per cent, 95 per cent and 99.7 per cent of SDSS galaxies from Mannucci et al. (2010). The blue dot–dashed line is the best fit to the SDSS galaxies.

offset between the SNe Ia hosts and best fit from SDSS galaxies is 0.005 ± 0.011 dex.

In summary, by examining both the mass–metallicity relation and FMR of SN Ia host galaxies, we find good agreement with the same relations derived from field galaxies, suggesting SN Ia host galaxies and normal field galaxies follow similar relations. This in turn suggests that the effect of metallicity on the SN Ia rate must be small.

5.3 The effect of metallicity on SN Ia luminosities

The peak luminosity of SNe Ia is powered by the radioactive decay of ^{56}Ni synthesized during the explosion. Timmes, Brown & Truran (2003) showed that the observed scatter in metallicity could introduce a 25 per cent variation in the mass of ^{56}Ni synthesized by SNe Ia. Metal-rich stars tend to synthesize more neutron-rich (and stable) ^{58}Ni instead of the ^{56}Ni that powers the SN Ia luminosity. As a result, and all other variables being equal, intrinsically fainter SNe Ia are expected to explode in higher metallicity environments.

However, Bravo & Badenes (2011) showed that SN Ia metallicities can be reasonably estimated by the host galaxy metallicity, and are better represented by gas-phase metallicity than by stellar metallicity. In this study, we used the host gas-phase metallicity as a proxy for the progenitor metallicity to study the metallicity effects on SNe Ia. Fig. 18 shows the dependence of Hubble residuals on metallicities based on different calibrations. Again, the relative metallicity conversions were not applied here, therefore the number of hosts which are available for different metallicity calibrations could be different. The results showed a good consistency between different calibrations. The slopes range from -0.74 to -1.13, with the Pearson correlation coefficients range from -0.42 to -0.51.

This suggests that the correlation between Hubble residual and gas-phase metallicity is independent of the calibration methods at least at the level of precision probed here.

Followed the procedure described in Hook et al. (1994), the Kendall rank correlation coefficients between Hubble residual, gas-phase metallicity, $M_{\rm stellar}$ and stellar age are listed in Table 8. Our results show that the SN Ia luminosity has the strongest dependence on the host gas-phase metallicity compared to $M_{\rm stellar}$ or stellar age. We also found that the correlation coefficient between Hubble residuals and $M_{\rm stellar}$ is similar to the value multiplicatively combining the correlation coefficients of the Hubble residual–metallicity and $M_{\rm stellar}$–metallicity relations, from which it can be inferred that the correlation between Hubble residuals and $M_{\rm stellar}$ may be a consequence of the Hubble residual–metallicity relation and the strong correlation between $M_{\rm stellar}$ and metallicity.

Hayden et al. (2013) applied the FMR to the SN Ia host galaxies using broad-band colours alone. They found the scatter of Hubble residual is greatly reduced by using the FMR instead of just the $M_{\rm stellar}$, which in turn implies that metallicity may be the underlying cause of the correlation between Hubble residual and $M_{\rm stellar}$. By directly measuring the gas-phase metallicity of SN Ia host galaxies, we can also show that it has a more significant effect on SN Ia luminosity than $M_{\rm stellar}$ or stellar age.

5.4 The SN Ia intrinsic colour

In Section 4.2, we examined the correlations between SN colour and host parameters, and found that the SNe Ia in high-metallicity and/or low-sSFR hosts appear to be redder. However, the SN colour discussed here (SIFTO $\mathcal{C}$) is not an 'intrinsic' SN colour, as dust extinction from the host galaxy may also contribute to the observed SN colour variation. Therefore, it is useful to compare the SN colour
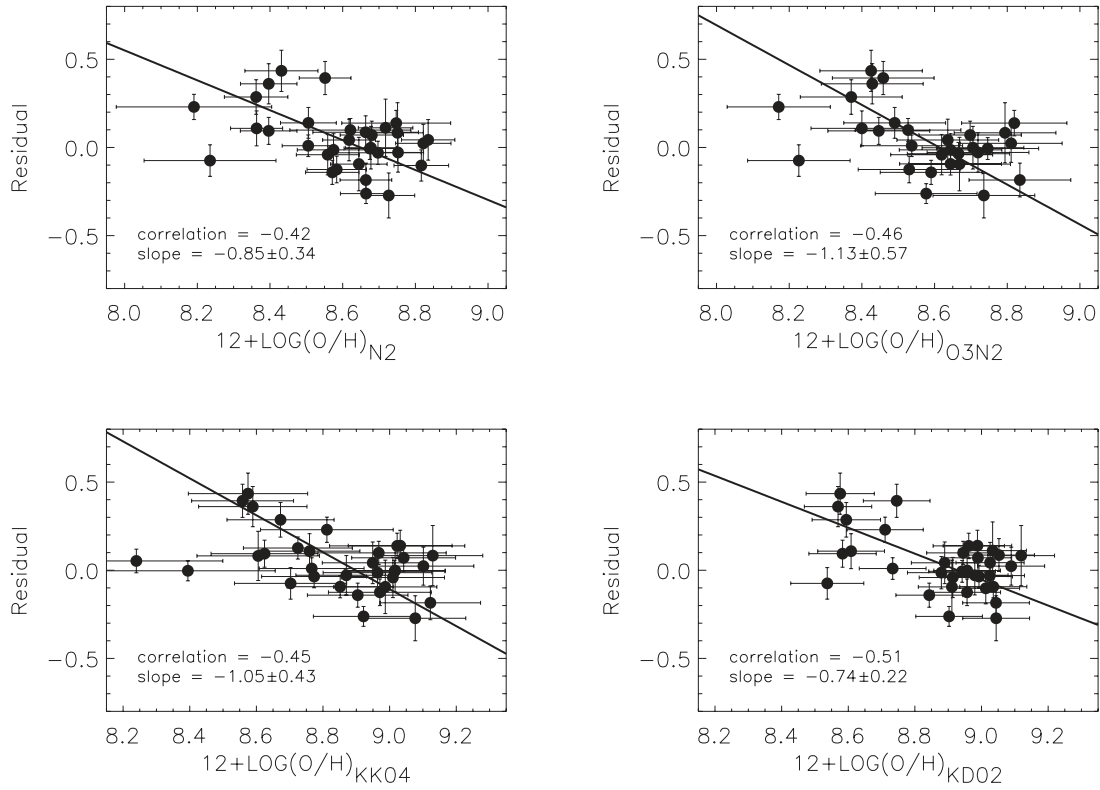
Figure 18. The Hubble residuals as function of host galaxy gas-phase metallicity using four different calibrations. The best linear fit is shown in solid line in each panel.

Table 8. Kendall rank correlation coefficients between Hubble residual (HR), gas-phase metallicity, $M_{stellar}$ and stellar age.

	HR	12+log (O/H)	$M_{stellar}$	Age
HR	–	−0.22	−0.13	−0.04
12+log (O/H)		–	0.49	0.03
$M_{stellar}$			–	0.35
Age				–

measures to independent measures of host extinction to assess the effect of dust extinction from the host galaxies.

Fig. 19 shows the host colour excess $E(B - V)$ determined from the Balmer decrement as function of host parameters and SN colour. Mild correlations between $E(B - V)$ and the gas-phase metallicity/sSFR are found, with Pearson correlation coefficients of 0.39 and 0.36 for gas-phase metallicity and sSFR, respectively. However, we see no significant correlation with SN colour: the SN colour appears independent of the host galaxy $E(B - V)$. This independence become even more evident when including those red SNe Ia with $C > 0.4$ previously excluded in this study.

There are two possibilities that could cause this. The first is that the bulk of the SN Ia colour variation is intrinsic to the SN event. Previous studies have shown that the SN Ia intrinsic colour could be altered systematically by changing the metallicity of the progenitor (Hoeflich et al. 1998; Domínguez, Höflich & Straniero 2001). There is some observational evidence for this: Childress et al. (2013b) recently showed that SNe Ia in high-metallicity hosts appear redder, and we also find a similar depen-

dence of SN Ia colour on host gas-phase and stellar metallicities in Fig. 10.

A second possibility is that there is dust local to the SN explosion that affects the colour, for example circumstellar dust (Wang 2005; Goobar 2008; Amanullah & Goobar 2011), but would not be traced by photons emerging from H II regions in the host galaxy. This interpretation is supported by evidence that the $B - V$ colour at maximum of SNe Ia correlates with the strength of narrow, blueshifted Na I D features in SN Ia spectra (Förster et al. 2013; Maguire et al. 2013), which likely trace the presence of circumstellar material (Patat et al. 2007; Sternberg et al. 2011).

6 CONCLUSIONS

In this paper, we have derived the parameters of a sample of 82 SN Ia host galaxies from the PTF, and used it to examine the relationships between SNe Ia and their hosts. The host galaxy parameters have been determined from both photometric and spectroscopic data. In particular, we have derived SFRs, stellar masses, gas-phase and stellar metallicities, and stellar ages for the host galaxies. Our main findings are as follows.

(i) Previously observed correlations between SN Ia properties and their host parameters are recovered in this work. In particular, we show that the SN light-curve width (stretch) has a strong dependence on host galaxy age and stellar mass – fainter, faster evolving (lower stretch) SNe Ia tend to be hosted by older, massive galaxies.

(ii) For the SN Ia colour, we have shown that redder SNe Ia have a tendency to explode in more metal-rich galaxies. However, we found no relation between SN colour and the colour excess of the
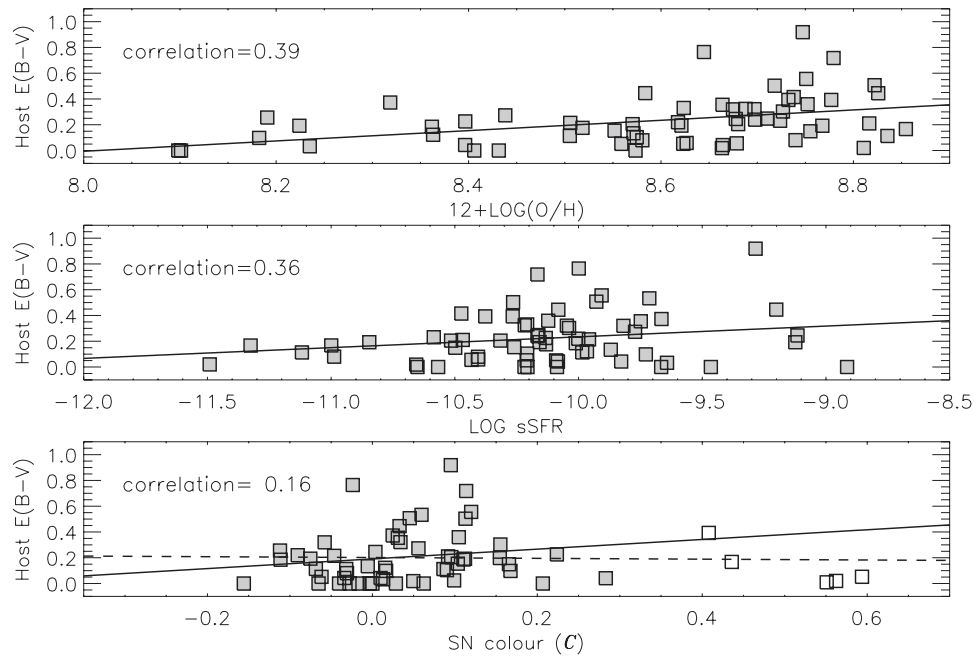
Figure 19. The colour excess of the host galaxies $E(B - V)$ as function of gas-phase metallicity, specific SFR and SN colour $\mathcal{C}$. The solid line in each panel represents the best linear fit to the data. The SNe with $\mathcal{C} > 0.4$ are shown in open squares in the lower panel, and the dashed line is the best linear fit to the data including these red SNe.

host galaxies as measured from the Balmer decrement, suggesting that the bulk of the SN Ia colour variation is intrinsic and not dependent on host galaxy extinction.

(iii) The dependence of the SN Ia Hubble residuals on host gas-phase metallicities was also confirmed. SNe Ia in metal-rich galaxies are ∼0.1 mag brighter than those in metal-poor galaxies after light-curve shape and colour corrections. This dependence does not depend on different metallicity calibrations. The correlation derived between Hubble residual and gas-phase metallicities is about two times stronger than for stellar mass. That implies that the host galaxy metallicity may be the underlying cause of the well-established relation between SN Ia luminosity and stellar mass.

(iv) We showed that the stellar mass distribution of the PTF and SNLS SN Ia host galaxies are quite different, with SNLS possessing many more low-mass host galaxies than PTF. However this can be understood and reproduced by a combination of a redshift-dependent GSMF, and an SN Ia rate inversely proportional to the age of the galaxy (a t^{-1} DTD).

(v) Finally, we compared the mass–metallicity relation for the SN Ia hosts to that of field galaxies drawn from SDSS. We found no significant difference between the two relations, a result that is not sensitive to the metallicity calibrations adopted. In addition, we derived the FMR (Mannucci et al. 2010) for the SN Ia hosts and also found it to be similar to that measured from field galaxies. This suggests that metallicity has a negligible effect on the SN Ia rate.

This study has emphasized the important role of the host galaxies of SNe Ia in influencing the SN explosion properties, with SN Ia properties showing considerable dependence on their host galaxy parameters. From a cosmological perspective, the precision of the cosmology can be improved by correcting these biases introduced by host galaxies. It can also shed light on the properties of SN Ia progenitors. Therefore, it is of great importance for future SN Ia surveys to study both the SNe and the galaxies in which they explode.

hemisphere, Chile, under programme IDs 084.A-0149 and 085.A-0777. Observations obtained with the SuperNova Integral Field Spectrograph on the University of Hawaii 2.2 m telescope as part of the Nearby Supernova Factory II project, a scientific collaboration between the Centre de Recherche Astronomique de Lyon, Institut de Physique Nucl'eaire de Lyon, Laboratoire de Physique Nucl'eaire et des Hautes Energies, Lawrence Berkeley National Laboratory, Yale University, University of Bonn, Max Planck Institute for Astrophysics, Tsinghua Center for Astrophysics and Centre de Physique des Particules de Marseille. This research has made use of the NASA/IPAC Extragalactic Database (NED) which is operated by the Jet Propulsion Laboratory, California Institute of Technology, under contract with the National Aeronautics and Space Administration.

This publication has been made possible by the participation of more than 10 000 volunteers in the Galaxy Zoo: Supernovae project (http://supernova.galaxyzoo.org/authors).

REFERENCES

Ahn C. P. et al., 2012, ApJS, 203, 21
Amanullah R., Goobar A., 2011, ApJ, 735, 20
Baldry I. K. et al., 2012, MNRAS, 421, 621
Baldwin J. A., Phillips M. M., Terlevich R., 1981, PASP, 93, 5
Bernstein J. P. et al., 2012, ApJ, 753, 152
Bertin E., Arnouts S., 1996, A&AS, 117, 393
Betoule M. et al., 2013, A&A, 552, A124
Bloom J. S. et al., 2012, PASP, 124, 1175
Bravo E., Badenes C., 2011, MNRAS, 414, 1592
Brinchmann J., Charlot S., White S. D. M., Tremonti C., Kauffmann G., Heckman T., Brinkmann J., 2004, MNRAS, 351, 1151
Brown T. M. et al., 2013, PASP, 125, 1031
Cappellari M., Emsellem E., 2004, PASP, 116, 138
Cardelli J. A., Clayton G. C., Mathis J. S., 1989, ApJ, 345, 245
Cenko S. B. et al., 2006, PASP, 118, 1396
Childress M. J. et al., 2013a, ApJ, 770, 107
Childress M. J. et al., 2013b, ApJ, 770, 108
Cid Fernandes R., Mateus A., Sodré L., Stasińska G., Gomes J. M., 2005, MNRAS, 358, 363
Conley A. et al., 2008, ApJ, 681, 482
Conley A. et al., 2011, ApJS, 192, 1
Cooper M. C., Newman J. A., Yan R., 2009, ApJ, 704, 687
D'Andrea C. B. et al., 2011, ApJ, 743, 172
Domínguez I., Höflich P., Straniero O., 2001, ApJ, 557, 279
Drory N. et al., 2009, ApJ, 707, 1595
Ellis R. S. et al., 2008, ApJ, 674, 51
Fioc M., Rocca-Volmerange B., 1997, A&A, 326, 950
Foley R. J. et al., 2008, ApJ, 684, 68
Foley R. J. et al., 2012, AJ, 143, 113
Förster F., González-Gaitán S., Folatelli G., Morrell N., 2013, ApJ, 772, 19
Foster C. et al., 2012, A&A, 547, A79
Gallagher J. S., Garnavich P. M., Berlind P., Challis P., Jha S., Kirshner R. P., 2005, ApJ, 634, 210
Gallagher J. S., Garnavich P. M., Caldwell N., Kirshner R. P., Jha S. W., Li W., Ganeshalingam M., Filippenko A. V., 2008, ApJ, 685, 752
Gallazzi A., Charlot S., Brinchmann J., White S. D. M., Tremonti C. A., 2005, MNRAS, 362, 41
Goobar A., 2008, ApJ, 686, L103
Gupta R. R. et al., 2011, ApJ, 740, 92
Guy J. et al., 2010, A&A, 523, A7
Guzman R., Gallego J., Koo D. C., Phillips A. C., Lowenthal J. D., Faber S. M., Illingworth G. D., Vogt N. P., 1997, ApJ, 489, 559
Hamuy M., Phillips M. M., Maza J., Suntzeff N. B., Schommer R. A., Aviles R., 1995, AJ, 109, 1
Hamuy M., Phillips M. M., Suntzeff N. B., Schommer R. A., Maza J., Aviles R., 1996, AJ, 112, 2391
Hamuy M., Trager S. C., Pinto P. A., Phillips M. M., Schommer R. A., Ivanov V., Suntzeff N. B., 2000, AJ, 120, 1479
Hayden B. T., Gupta R. R., Garnavich P. M., Mannucci F., Nichol R. C., Sako M., 2013, ApJ, 764, 191
Hoeflich P., Wheeler J. C., Thielemann F. K., 1998, ApJ, 495, 617
Hook I. M., McMahon R. G., Boyle B. J., Irwin M. J., 1994, MNRAS, 268, 305
Hook I. M., Jørgensen I., Allington-Smith J. R., Davies R. L., Metcalfe N., Murowinski R. G., Crampton D., 2004, PASP, 116, 425
Howell D. A., 2001, ApJ, 554, L193
Howell D. A. et al., 2009, ApJ, 691, 661
Ivezić Ž. et al., 2007, AJ, 134, 973
Johansson J. et al., 2013, MNRAS, 435, 1680
Kauffmann G. et al., 2003, MNRAS, 346, 1055
Kelly B. C., 2007, ApJ, 665, 1489
Kelly P. L., Hicken M., Burke D. L., Mandel K. S., Kirshner R. P., 2010, ApJ, 715, 743
Kennicutt J. R. C., 1998, ARA&A, 36, 189
Kessler R. et al., 2009, ApJS, 185, 32
Kewley L. J., Dopita M. A., 2002, ApJS, 142, 35 (KD02)
Kewley L. J., Ellison S. L., 2008, ApJ, 681, 1183 (KE08)
Kewley L. J., Dopita M. A., Sutherland R. S., Heisler C. A., Trevena J., 2001, ApJ, 556, 121
Kistler M. D., Stanek K. Z., Kochanek C. S., Prieto J. L., Thompson T. A., 2013, ApJ, 770, 88
Kobayashi C., Nomoto K., 2009, ApJ, 707, 1466
Kobayashi C., Tsujimoto T., Nomoto K., Hachisu I., Kato M., 1998, ApJ, 503, L155
Kobulnicky H. A., Kewley L. J., 2004, ApJ, 617, 240 (KK04)
Koleva M., Prugniel P., Bouchard A., Wu Y., 2009, A&A, 501, 1269
Kroupa P., 2001, MNRAS, 322, 231
Lampeitl H. et al., 2010, ApJ, 722, 566
Law N. M. et al., 2009, PASP, 121, 1395
Le Borgne D., Rocca-Volmerange B., 2002, A&A, 386, 446
Lentz E. J., Baron E., Branch D., Hauschildt P. H., Nugent P. E., 2000, ApJ, 530, 966
Maguire K. et al., 2012, MNRAS, 426, 2359
Maguire K. et al., 2013, MNRAS, 436, 222
Mannucci F., Della Valle M., Panagia N., Cappellaro E., Cresci G., Maiolino R., Petrosian A., Turatto M., 2005, A&A, 433, 807
Mannucci F., Della Valle M., Panagia N., 2006, MNRAS, 370, 773
Mannucci F., Cresci G., Maiolino R., Marconi A., Gnerucci A., 2010, MNRAS, 408, 2115
Maoz D., Mannucci F., 2012, Publ. Astron. Soc. Aust., 29, 447
Maraston C., 2005, MNRAS, 362, 799
Mazzali P. et al., 2013, preprint (arXiv:e-prints)
McGaugh S. S., 1991, ApJ, 380, 140 (M91)
Miller J. S., Stone R. P. S., 1993, Lick Observatory Technical Report No. 66, Univ. California, Santa Cruz, CA
Miller C. J., Nichol R. C., Gómez P. L., Hopkins A. M., Bernardi M., 2003, ApJ, 597, 142
Neill J. D. et al., 2009, ApJ, 707, 1449
Oke J. B. et al., 1995, PASP, 107, 375
Patat F. et al., 2007, Science, 317, 924
Perlmutter S. et al., 1999, ApJ, 517, 565
Perrett K. et al., 2010, AJ, 140, 518
Pettini M., Pagel B. E. J., 2004, MNRAS, 348, L59 (PP04)
Phillips M. M., 1993, ApJ, 413, L105
Press W. H., Teukolsky S. A., Vetterling W. T., Flannery B. P., 1992, Numerical recipes in FORTRAN: The Art of Scientific Computing. Cambridge Univ. Press, Cambridge
Rahmer G., Smith R., Velur V., Hale D., Law N., Bui K., Petrie H., Dekany R., 2008, McLean I. S., Casali M. M., eds, Proc. SPIE Vol. 7014, Ground-based and Airborne Instrumentation for Astronomy II. SPIE, Bellingham, p. 70144Y
Rau A. et al., 2009, PASP, 121, 1334
Riess A. G., Press W. H., Kirshner R. P., 1996, ApJ, 473, 88
Riess A. G. et al., 1998, AJ, 116, 1009

Riess A. G. et al., 1999, AJ, 117, 707
Riess A. G. et al., 2007, ApJ, 659, 98
Rigault M. et al., 2013, A&A, 560, A66
Salpeter E. E., 1955, ApJ, 121, 161
Sánchez-Blázquez P. et al., 2006, MNRAS, 371, 703
Sarzi M. et al., 2006, MNRAS, 366, 1151
Schlafly E. F., Finkbeiner D. P., 2011, ApJ, 737, 103
Shaw R. L., 1979, A&A, 76, 188
Smith J. A. et al., 2002, AJ, 123, 2121
Smith A. M. et al., 2011, MNRAS, 412, 1309
Smith M. et al., 2012, ApJ, 755, 61
Stanishev V., Rodrigues M., Mourão A., Flores H., 2012, A&A, 545, A58
Steele I. A. et al., 2004, in Oschmann J. M., Jr, ed., Proc. SPIE Vol. 5489,
    Ground-based Telescopes. SPIE, Bellingham, p. 679
Sternberg A. et al., 2011, Science, 333, 856
Sullivan M. et al., 2006, ApJ, 648, 868
Sullivan M. et al., 2010, MNRAS, 406, 782
Sullivan M. et al., 2011a, ApJ, 732, 118
Sullivan M. et al., 2011b, ApJ, 737, 102
Suzuki N. et al., 2012, ApJ, 746, 85
Timmes F. X., Brown E. F., Truran J. W., 2003, ApJ, 590, L83
Trager S. C., Worthey G., Faber S. M., Burstein D., Gonzalez J. J., 1998,
    ApJS, 116, 1
Tremonti C. A. et al., 2004, ApJ, 613, 898
Tripp R., 1998, A&A, 331, 815
van Dokkum P. G., 2001, PASP, 113, 1420
Vazdekis A., Sánchez-Blázquez P., Falcón-Barroso J., Cenarro A. J., Beasley
    M. A., Cardiel N., Gorgas J., Peletier R. F., 2010, MNRAS, 404, 1639
Wang L., 2005, ApJ, 635, L33
Worthey G., 1994, ApJS, 95, 107
Yaron O., Gal-Yam A., 2012, PASP, 124, 668

This paper has been typeset from a TeX/LaTeX file prepared by the author.